CHARACTERIZATION OF THE PARTICLE SIZE DISTRIBUTION, MINERALOGY AND FE MODE OF OCCURRENCE OF DUST-EMITTING SEDIMENTS FROM THE MOJAVE DESERT, CALIFORNIA, USA

Adolfo González-Romero[1,2,3], Cristina González-Flórez[1,3], Agnesh Panta[4], Jesús Yus-Díez[5], Patricia Córdoba[2], Andres Alastuey[2], Natalia Moreno[2], Melani Hernández-Chiriboga[1], Konrad Kandler[4], Martina Klose[6], Roger N. Clark[7], Bethany L. Ehlmann[8], Rebecca N. Greenberger[8], Abigail M. Keebler[8], Phil Brodrick[9], Robert Green[9], Paul Ginoux[10], Xavier Querol[2], Carlos Pérez García-Pando[1,11]

[1] Barcelona Supercomputing Center (BSC), Barcelona, Spain
[2] Spanish Research Council, Institute of Environmental Assessment and water Research (IDAEA-CSIC), Barcelona, Spain
[3] Polytechnical University of Catalonia (UPC), Barcelona, Spain
[4] Institute of Applied Geosciences, Technical University Darmstadt, Darmstadt, Germany
[5] Centre for Atmospheric Research, University of Nova Gorica, Ajdovščina, Slovenia.
[6] Karlsruhe Institute of Technology (KIT), Institute of Meteorology and Climate Research Troposphere Research (IMKTRO), Karlsruhe, Germany
[7] PSI Planetary Science Institute, Tucson, AZ, USA
[8] California Institute of Technology, Division of Geological and Planetary Sciences, Pasadena, CA, USA
[9] Jet Propulsion Laboratory, California Institute of Technology
[10] NOAA Geophysical Fluid Dynamics Laboratory, Princeton, NJ, USA
[11] Catalan Institution for Research and Advanced Studies (ICREA), Barcelona, Spain

Corresponding author: Adolfo González-Romero (agonzal3@bsc.es) and Xavier Querol (xavier.querol@idaea.csic.es)

Abstract

Constraining dust models to understand and quantify the effect of dust upon climate and ecosystems requires comprehensive analyses of the physiochemical properties of dust-emitting sediments in arid regions. Building upon previous studies in the Moroccan Sahara and Iceland, we analyse a diverse set of crusts and aeolian ripples (n=55) from various potential dust-emitting basins within the Mojave Desert, California, USA. Our focus is on characterizing particle size distribution (PSD), mineralogy, aggregation/cohesion state and Fe mode of occurrence. Our results show differences in fully and minimally dispersed PSDs, with crusts exhibiting average median diameters of 92 and 37 μm, respectively, compared to aeolian ripples with 226 and 213 μm, respectively. Mineralogical analyses unveiled strong variations between crusts and ripples, with crusts being enriched in phyllosilicates (24 vs 7.8 %), carbonates (6.6 vs 1.1 %), Na-salts (7.3 vs 1.1 %) and zeolites (1.2 and 0.12 %), and ripples being enriched in feldspars (48 vs 37 %), quartz (32 vs 16 %), and gypsum (4.7 vs 3.1 %). The size fractions from crust sediments display a homogeneous mineralogy, whereas those of aeolian ripples more heterogeneity, mostly due to different particle aggregation. Bulk Fe content analyses indicate higher concentrations in crusts (3.0±1.3 wt %) compared to ripples (1.9±1.1 wt %), with similar proportions in their Fe mode of occurrence: nano Fe-oxides/readily exchangeable Fe represent ~1.6 %, hematite/goethite ~15 %, magnetite/maghemite ~2.0 % and structural Fe in silicates ~80 % of the total Fe. We identified segregation patterns in PSD and mineralogy differences in Na-salts content within the Mojave basins, which can be explained by sediment transportation dynamics and precipitates due to groundwater table fluctuations described in previous studies in the region. Mojave Desert crusts show similarities with previously sampled crusts in the Moroccan Sahara in terms of PSD and readily exchangeable Fe, yet exhibit substantial differences in mineralogical composition, which should significantly influence the characteristic of the emitted dust particles.

Keywords: Arid regions, dust sources, desert dust, dust-emitting sediment formation model, dust mineralogy.

1. Introduction

Desert dust produced by wind erosion of arid and semi-arid surfaces has significant effects on climate, ecosystems and health (Weaver et al., 2002; Goudie & Middleton, 2006; Sullivan et al., 2007; Crumeyrolle et al., 2008; De Longeville et al., 2010; Karanasiou et al., 2012; Pérez García-Pando et al., 2014; among others). Dust affects the energy and water cycles through its absorption and scattering of both shortwave (SW) and longwave (LW) radiation (Perez et al., 2006; Miller et al., 2014), and exerts influence on cloud formation, precipitation patterns, and the associated indirect radiative forcing by serving as nuclei for liquid and ice clouds (e.g. Harrison et al., 2019). Dust also undergoes heterogeneous chemical reactions in the atmosphere that enhance their hygroscopicity and modify their optical properties (Bauer et al., 2005), and when deposited into ocean waters, its bioavailable iron content acts as a catalyst for photosynthesis by ocean phytoplankton, thereby increasing carbon dioxide uptake and influencing the global carbon cycle (Jickells et al., 2005). Dust primarily originates from arid inland basins, which include various sedimentary environments such as aeolian deposits, endorheic depressions, and fluvial- and alluvial-dominated systems (Bullard et al., 2011). Wind typically mobilizes loose sand from adjacent ripples or dunes, which then erodes more consolidated surfaces, typically paved sediments and crusts, to release dust (Stout and Lee, 2003; Shao et al., 2011). Atmospheric dust emission models have improved by identifying preferential dust sources using criteria like topography and hydrology (Ginoux et al., 2001). However, these models still struggle with capturing small-scale variability partly due to the lack of relevant soil measurements in arid regions, despite advancements in understanding the geomorphological and sedimentological factors influencing dust emissions (Bullard et al., 2011). For instance, the particle size distribution (PSD) and cohesion of the sediments affect saltation bombardment and aggregate disintegration processes involved in dust emission (Shao et al., 1993).

Understanding the mineral composition of dust is also crucial for assessing its climate impact. Dust contains various minerals such as quartz, clay minerals, feldspars, carbonates, salts, and iron oxides. The climate effects of dust are influenced by these minerals' relative abundances, sizes, shapes, and mixing states. For example, iron oxides control solar radiation absorption by dust (Formenti et al., 2014; Engelbrecht et al., 2016; Di Biagio et al., 2019; Zubko et al., 2019), nano Fe oxides and easily exchangeable Fe increase the fertilising effect of dust in ocean and terrestrial ecosystems (Hettiarachchi et al., 2019; Baldo et al., 2020, Hettiarachchi et al., 2020), K-feldspar and quartz impact ice nucleation in clouds (Atkinson et al., 2013; Harrison et al., 2019; Chatziparaschos et al., 2023), and calcite influences acid reactions on dust surfaces (Paulot et al., 2016). The mineralogical composition of dust can vary significantly across different regions due to geological and climatic factors (Claquin et al., 1999; Journet et al., 2014). However, most models assume a globally uniform dust composition due to limited global data on parent soil sources. Only a few models account for dust mineralogical composition variations (e.g., Scanza et al., 2015; Perlwitz et al., 2015; Li et al., 2021; Gonçalves Ageitos et al., 2023; Obiso et al., 2024) by using global soil type atlases that are based on the extrapolation of a limited number of soil analyses (Claquin et al., 1999; Journet et al., 2014). These atlases rely on assumptions about soil texture and colour, often base their data on soil samples taken from depths deeper than those relevant to wind erosion, and the method used to characterize particle size and associated mineralogy fully breaks down natural soil aggregates.

Since 2022, the EMIT mission has been acquiring comprehensive measurements of surface mineralogical composition for use in Earth System models (Green et al., 2020). EMIT employs imaging

spectroscopy across the visible to short wavelength infrared (VSWIR) spectral range from the International Space Station to map the occurrence and estimate the abundance of ten key dust source minerals. Additionally, EMIT has the potential to estimate surface soil texture. While identifying dominant surface minerals has traditionally been a strength of spectrometers, quantifying these minerals poses significant challenges. Factors such as mineral grain size and composition can affect spectral absorptions, certain dominant materials like quartz and feldspar exhibit minimal absorption features, and the presence of other materials can further complicate the analysis.

Overall, there is a notable lack of comprehensive measurements characterizing relevant properties of surface sediments in dust source regions. This gap hampers our ability to evaluate and constrain mineral abundance derived from reflectance spectroscopy and to improve dust emission modeling. Addressing this issue, the FRontiers in dust minerAloGical coMposition and its Effects upoN climaTe (FRAGMENT) project has, over recent years, conducted a series of coordinated and interdisciplinary field campaigns across remote dust source regions. The project's objectives include enhancing the understanding and quantification of dust-source properties, examining their relationship with emitted dust characteristics, refining spaceborne spectroscopy retrievals of surface minerals (Green et al., 2020, Clark et al., 2024), and improving the representation of dust mineralogy in Earth system models (Perlwitz et al., 2015; Li et al., 2021; Gonçalves et al., 2023; Obiso et al., 2023). The FRAGMENT field campaigns involved regional sediment sampling in several regions and detailed wind erosion and dust emission measurements at selected sites. Studies stemming from these activities include those by González-Romero et al. (2023), González-Flórez et al. (2022), and Panta et al. (2022), and González-Romero et al. (2024). These campaigns have been executed in various geographic locations, such as the Moroccan Sahara (2019), Iceland (2021), the Mojave Desert in the United States (2022), and Jordan (2022). Through these efforts, the FRAGMENT project contributes to filling critical knowledge gaps in dust-source characterization.

Following our previous studies in the Moroccan Sahara (González-Romero et al. 2023) and Iceland González-Romero et al. (2024), this study focuses on the characterization of dust-emitting sediments collected from the Mojave Desert in 2022. The Mojave Desert is a closed-basin wedge-shaped region located in the southwestern United States, between California and Nevada. The region is surrounded by mountain ranges and traversed by the Mojave river and other intermittent rivers for over 200 km from the San Bernardino mountains to the east (Dibblee, 1967, Reheis et al., 2012). Despite its limited global importance (dust emission from North America represents only ~3 % of the global dust emission; Kok et al., 2021), the Mojave Desert is an important regional dust source (Ginoux et al., 2012), with most emission occurring in the playa lakes and alluvium deposits near playa lakes (Reheis & Kihl, 1995; Reheis et al. 2009, Urban et al., 2018). Reynolds et al. (2009) observed 71 days with dust plumes during 37 months of camera recording at the Franklin Lake playa. According to remote sensing data (MODIS), aerosol optical depth (AOD) is higher in spring and summer and reaches a minimum in winter (Frank et al., 2007). However, from November to May, eastward flows of the jet-stream affect the Mojave Desert, which, in combination with topography, favour the development of northerly winds that can lead to dust emission (Urban et al., 2009). Up to 65 % of emission in the Mojave Desert is estimated to be due to natural factors, whereas 35 % to anthropogenic activities, including off-road recreation practices, mine operations, and military training and livestock grazing (Frank et al., 2007). The AOD in this region is also affected by dust transported from other regions (Tong et al., 2012) and pollution transported from the Los Angeles Basin (Frank et al., 2007, Urban et al., 2009). In the Mojave

157 Desert, Reynolds et al. (2009) noted an association between wet periods and dust emission, directly
158 related to the generation of new thin crusts and salt crust removal.

159 The Mojave Desert includes several significant playa lakes, such as Rogers and Rosemond, Owens Lake,
160 Death-Valley-Badwater, Panamint Valley, Bristol, Cadiz and Danby, Searles Lake, Soda Lake, and
161 Mesquite Lake, among others (Reheis & Kihl, 1995; Reheis, 1997; Potter and Coppernoll-Houston,
162 2019). Reynolds et al. (2007 and 2009) distinguished between two types of playa lakes: wet playas
163 influenced by groundwater, and dry playas, unaffected by groundwater, though both can experience
164 surface-water runoff. Goudie (2018) further delineated wet playas as having a groundwater table
165 within 5 m of the surface, while dry playas have a groundwater table deeper than 5 m. Additionally,
166 Goudie (2018), Buck et al. (2011), Nield et al. (2015) and Nield et al. (2016) observed that the
167 interaction between salt minerals and the groundwater table on wet playas lead to the formation of
168 fluffy surfaces through salt reworking by water during evapotranspiration.

169 In the Mojave Desert, three different Aridisols are present in the Rand mountains alluvial fan,
170 corresponding to Xerillic soils or Aridisols according to Eghbal & Southard (1993), which are typical in
171 arid and semi-arid regions, with low organic matter content and low structures. The uppermost layer
172 of those Aridisols, ranging from 0 to 1 cm in depth exhibited a texture of 15-30% gravel, 69-74 % sand
173 and 10-11 % clay. Reheis et al. (1995) described soils (<2 mm) primarily composed of silt (30-70 %) and
174 clay (20-45 %). The mineralogy of those samples was dominated by quartz, feldspars, amphiboles, and
175 clay minerals, including smectite, mica and kaolinite (Eghbal & Southard, 1993). The Cronese Lakes
176 and Soda Lake playas are documented to contain salt precipitates, but mineralogy is not specified.
177 Mesquite Lake playa is noted for its gypsum deposits (Reynolds et al., 2009). At Franklin Lake playa,
178 surfaces are characterised by silt-clay size particles (Goldstein et al., 2017) with mineralogical
179 descriptions provided in Reynolds et al. (2009) indicating fluffy surfaces comprised of halite,
180 thenardite, trona, burkeite, calcite, illite, smectite, and kaolinite. Similar mineralogical results are
181 described at Soda Lake by Reheis et al. (2009), with a higher proportion of Na-salts, quartz, gypsum
182 and carbonates. Furthermore, Goldstein et al. (2017) identified a diverse array of minerals at Franklin
183 Lake playa, including clays, zeolites, plagioclase, K-feldspar, quartz, calcite, dolomite and salt minerals
184 such as trona, halite, burkeite and thenardite.

185 This study characterises the particle size distribution, mineralogy and modes of occurrence of Fe of
186 selected potential dust-emitting sediment surfaces from the Mojave Desert. In addition, the
187 mineralogy of different size fractions is analysed, based on a sieving protocol that minimally disturbs
188 sediments. We further discuss the potential effect of sedimentary transport on the particle size and
189 mineralogy across the sampled basins building upon previous studies in the literature. Finally, our
190 results are broadly compared with current EMIT standard (semi-quantitative) products, and with those
191 obtained using similar protocols in previous FRAGMENT campaigns in other regions (González-Romero
192 et al., 2023; González-Romero et al., 2024).

2. Methodology

2.1 Study area

195 The Mojave Desert, located between California and Nevada, has a diverse geological history spanning
196 from the Cambrian and Precambrian eras to the Holocene (Figure 1). This geological complexity

197 encompasses volcanic, plutonic, metamorphic, and sedimentary units (Jennings et al., 1962; Miller et
198 al., 2014). In areas once submerged during the last glacial maximum (LGM), we now find ephemeral
199 playa lakes that have existed for thousands of years since the LGM, offering a glimpse into the region's
200 dynamic past (Miller et al., 2018). These playa lakes together with alluvial fans, floodplains and other
201 features are surrounded by a variety of source rocks, exhibit diverse particle sizes and compositions
202 and can potentially emit dust under favourable wind conditions.

203 The regional distribution of the annual Frequency of Occurrence (FoO) of dust events with dust optical
204 depth exceeding 0.1, derived from MODIS Deep Blue C6.1 Level 2 data following the methodology of
205 Ginoux et al. (2012), is illustrated in Figure 2. The FoO provides an overall estimate of dust emission
206 frequency above a certain threshold at a resolution of 0.1º by 0.1º over the region. Sediment samples
207 were collected from various locations within the Mojave Desert region, including areas with relatively
208 high FoO (see locations in Figures 1 and 2). Among these locations is Soda Lake and its surroundings,
209 near Baker, CA, which is linked to Silver Lake to the north and is surrounded by igneous, volcanic, and
210 carbonate rocks, as well as dune fields to the south (Figure 1). The area is influenced by aeolian,
211 alluvial, and fluvial processes and experiences annual precipitation of 80-100 mm (Urban et al., 2018).
212 This ephemeral lake contains salts resulting from the evaporation of groundwater sourced from an
213 aquifer nestled in the Zzyzx Mountains (Honke et al., 2019). Dust emissions are a recurrent
214 phenomenon, originating from fine sediments accumulated in the lake's central areas during sporadic
215 floodings, from the white evaporite surfaces in the lake, and from the alluvial deposits to the south of
216 the playa lake (Urban et al., 2018). According to the FoO, the areas with higher dust emissions are the
217 southern part of the lake and the alluvial deposits to the southwest, extending up to Afton Canyon.

218 Samples were also collected from the Cronese lakes, Mesquite Lake, Ivanpah Lake and Coyote Lake
219 (Figure 1), which lie in areas with significant FoO signals (Figure 2) and have been documented as dust
220 sources in Reheis & Kihl (1995) and Reheis et al. (2009). The Cronese lakes are adjacent to the Soda
221 Lake area to the west, sharing a similar geologic context (Figures 1 and 2). Mesquite Lake, located on
222 the border between California and Nevada, is encircled by carbonate and igneous rocks, mirroring the
223 geological setting of the nearby Ivanpah Lake. Notably, Mesquite Lake playa is the only playa affected
224 by a gypsum mine pit, as documented by Reynolds et al. (2009). Further contributing to the diversity
225 of the region's geological makeup is Coyote Lake, flanked by Miocene and Pleistocene sediments.
226 These playa lakes, characterised as endorheic ephemeral lakes, receive groundwater inputs in some
227 cases, enriching the lakes with salts that subsequently precipitate on the surfaces of their central
228 regions (Whitney et al., 2015; Urban et al., 2018).

229 Other areas with relatively high FoO not sampled in our study include the Ashford Junction alluvial
230 deposits and the Fort Irwin area, where the northern valley, including Nelson Lake, may be more prone
231 to dust emission due to significant anthropogenic disturbance. It is important to note that the FoO
232 may tend to highlight areas such as playas and their surroundings, where in some cases the most dust
233 per unit area could be produced (Floyd and Gill, 2011; Baddock et al., 2016). However, some alluvial
234 regions with lower emission rates not surpassing the FoO threshold may produce more dust overall
235 due to their greater areal extent (Reheis and Kihl, 1995; Baddock et al., 2016). Additionally, many other
236 types of dust-producing surfaces active in the Mojave Desert, such as gravel roads, agricultural lands,
237 and recreational off-road tracks, are rarely observed by satellite retrievals (Urban et al., 2018).

The new EMIT sensor onboard the International Space Station offers a glimpse of the mineralogical diversity in the Mojave Desert (Green et al., 2020). Figure 3 displays standard Tetracorder RGB color composite semi-quantitative products for EMIT. Tetracorder is a software system that employs a set of algorithms within an expert system decision-making framework to identify and map compounds (Clark, 2024; Clark et al., 2024). Figure 3 shows a true color image, along with standard products for Fe^{2+} and Fe^{3+} bearing mineral electronic absorptions (including hematite and goethite) in the visible to very-near infrared spectral range. It also displays standard products for the EMIT-targeted minerals, excluding hematite and goethite: calcite, chlorite/serpentine, dolomite, gypsum, illite/muscovite, kaolinite-dioctahedral group, montmorillonite group, and vermiculite. These products highlight areas where the presence of each mineral or component is significant, measured in terms of band depth*fit, where the fit represents the least squares correlation coefficient from a feature fit of observed and reference library spectra. These analyses reveal the widespread presence of phyllosilicates such as kaolinite, smectite, montmorillonite, and illite across the area. The northeastern sector, particularly around Mesquite Lake, exhibits notable concentrations of carbonates and gypsum. Additionally, goethite and hematite are detected, with a more pronounced presence of goethite in the northern portion and hematite in the southern part of the region. The detection of mixtures of Fe^{2+} and Fe^{3+} within various minerals enriches our understanding of the region's mineralogical diversity.

Quantitative surface mineralogy (mineral mass abundances of the 10 EMIT-targeted minerals) and soil texture products are currently being developed by the EMIT team for use in Earth System Models. Their publication and evaluation will be the focus of forthcoming publications. Thus, it is beyond the scope of this study to perform a detailed quantitative comparison between our analyses and comparable EMIT products. However, in the results section, we broadly compare these standard products with the results of our in-situ analyses.

2.2 Sampling

Representative surfaces of dust-emitting sediments were sampled in May 2022, with depths of up to 3 cm, using a 5 cm2 inox shovel. Samples were stored in a plastic bag, labelled, and documented with photographs, descriptions, and coordinates, and transported to the laboratories for subsequent analyses. The type of samples considered are crusts (semi-cohesive fine sediments accumulated during floodings in depressions) and ripples (aeolian ripples that are built up under favorable winds and supply sand for saltation) (Figure 4). A total of 55 surface sediments and ripples (32 from Soda Lake, 9 from Mesquite Lake, 1 from Ivanpah Lake, 11 from the Cronese Lakes, and 2 from Coyote Lake) were sampled for laboratory analysis. Once in the laboratory, the samples were dried for 24-48 h at 40-50 ºC, sieved to pass through a 2 mm mesh.

Our rationale for selecting crusts and ripples is two-fold. On the one side, dust emission is primarily driven by two mechanisms: saltation bombardment and aggregate disintegration. In saltation bombardment, dust is ejected from soil aggregates (typically crusts and paved sediments rich in clay and silt particles) when impacted by saltating sand particles. In aggregate disintegration, dust is released from saltating soil aggregates (Shao et al., 1993; Alfaro et al., 1997; Shao, 2001). By characterizing the PSD (both dry and wet sieved) and mineralogy of ripples (concentrating sand particles) and crusts (concentrating clay and silt particles), we provide comprehensive and valuable information for developing and refining dust emission models. On the other side, in arid regions, quartz and feldspar typically dominate sediment mass. However, current spaceborne hyperspectral

280 instruments (such as EMIT) cannot directly identify feldspar and quartz because their absorption
281 features lie outside the instrument's spectral range. This poses a significant challenge in quantifying
282 surface mineral abundances from remote spectroscopy. At all FRAGMENT sampling locations
283 (Morocco, Iceland, US-Mojave, and Jordan), we measured reflectance spectra using an ASD Fieldspec
284 3. By characterizing and contrasting ripples (with high quartz and feldspar content and larger particle
285 sizes) and crusts, we aim to provide information to enhance understanding and improve modelling
286 assumptions for estimating surface mineral abundances and soil texture from remote spectroscopy in
287 subsequent studies.

288 We acknowledge that the limited number of samples collected may not fully represent the potential
289 variability among crusts and ripples within the studied locations due to varying conditions (Buck et al.,
290 2011). However, our samples broadly represent the composition and particle size distributions (PSDs)
291 of this type of sediments in these areas, allowing for meaningful comparisons with sediments from
292 other locations.

293 **2.3 Analyses**

294 2.3.1 Particle size distribution

295 Particle size distributions (PSD) of bulk samples (<2 mm) were analysed as described in González-
296 Romero et al. (2023) for the evaluation of the aggregation state. First, we conducted a minimally
297 dispersed PSD (MDPSD) analysis, which minimizes the breaking of the aggregates that are
298 encountered in natural conditions. Second, we conducted a fully dispersed PSD (FDPSD) analysis,
299 which breaks the aggregates. Wet dispersion was done according to Sperazza et al. (2004), using water
300 and sodium hexametaphosphate dispersion for 24 h. Both PSDs (MDPSD and FDPSD) were obtained
301 by a laser diffractometer with the Malvern Mastersizer 2000 Hydro G and Scirocco for the fully and
302 minimally dispersed conditions, respectively. We note that under wet dispersion, at least some salt
303 minerals may dissolve.

304 In addition, we separated 20 selected samples from different sources, including 16 crusts and 4 aeolian
305 ripples, into different size ranges to understand how mineral composition changes with size. We used
306 a series of sieves with mesh sizes of 2 mm, 1 mm, 500 µm, 250 µm, 80 µm, 63 µm, 40 µm, and 20 µm.
307 The sieving process involved hand shaking the full column for 1 minute, followed by ultrasound
308 sonication for 1 minute at the 500 µm, 80 µm, 40 µm, and 20 µm size fractions. This method ensured
309 the effective separation of the size fractions for subsequent mineralogical analysis.

310 2.3.2 Mineralogical composition

311 To quantify the different contents of crystalline minerals and amorphous components, X-Ray
312 Diffraction (XRD) coupled with a Rietveld quantitative method were used (Rietveld, 1969; Cheary and
313 Coelho, 1992; Young, 1995 and Topas, 2018). Adding a known amount of an internal standard material
314 allowed, via the Rietveld method, the quantification of a mixture of minerals and any non-crystalline
315 material in the mixture not included in the Rietveld method (De la Torre et al., 2001; Madsen, 2001,
316 Scarlett and Madsen, 2006; Machiels et al., 2010; Ibañez et al., 2013). For the analysis, a measured
317 amount of dry ground sample was mixed and dry ground again with 10-20 % of fluorite (CaF$_2$ powder,
318 Merck), used here as an internal standard for quantitative purposes. The XRD patterns of the samples

were analysed by a Bruker D8 A25 Advanced Powder X-ray diffractometer operated at 40kV and 40 mA with monochromatic Cu Kα radiation (=1,5405 Å). This device uses a Bragg-Brentano geometry and a sensitive detector LynxEye 1D. Diffractograms were recorded from 4 to 120º of 2θ and steps of 0.015º in 1s and maintained rotation (15/min). For the clay identification, samples were analysed using the oriented aggregate method by XRD, decanting clay fractions from samples and smearing the slurries in glass slides. After, three treatments were applied including air drying (AO), glycolation with ethylene glycol (AG) and heating at 550 ºC for 2h (AC) with its three different diffractograms. Finally, the three diffractograms allows to corroborate the presence of Illite, Chlorite, Palygorskite and Montmorillonite through Thorez (1976) and USGS Open File procedures. Data collected were evaluated using the Bruker AXS DIFFRAC.EVA software package (Bruker AXS, Karlsruhe, Germany, 2000) and the Rietveld analyses performed with TOPAS 4.2 program (Bruker AXS, 2003-2009). A Chebyshev function of level 5 was used to fit the background and abundances of crystalline and amorphous phases were normalised to 100 %. Fits were evaluated by visual comparison, R_{wp} (R-weighted pattern), R_{exp} (R-expected), and Goodness of Fit (GOF).

2.3.3 Mode of occurrence of Fe

As XRD is not precise enough for Fe-oxide quantification, wet chemistry and sequential extractions of Fe are needed for quantification of the mode of occurrence of Fe (González-Romero et al., 2023; 2024). Samples were analysed with a two-step acid digestion for the total Fe (FeT) content following Querol et al. (1993, 1997). A reference material (NIST-1633b, coal fly ash) was used for quality control in every batch. The sequential extraction presented in Shi et al. (2009), Baldo et al. (2020) and González-Romero et al. (2024) were used to quantify readily exchangeable Fe ions and nano Fe oxides (FeA), the amount of crystalline Fe oxides as goethite and hematite (FeD), and crystalline magnetite (FeM). For the first extraction, 30 mg sample were leached with 10 ml of an ascorbate solution (extractant solution) and shaken in dark conditions for 24 h and filtered. Another 30 mg were leached with 10 ml of a dithionite solution (extractant solution), shaken for 2 h in dark conditions and filtered for the second extraction. The solid residue was then leached again in 10 ml of an oxalate solution for 6 h in dark conditions and filtered for the third extraction. The extracted solution of each phase (FeT, FeA, FeD and FeM) was analysed to quantify dissolved Fe by Inductively Coupled Plasma Atomic Emission Spectrometry (ICP-AES). FeA is obtained with the first extraction, FeD is obtained subtracting from the second extraction the amount of Fe from the first extraction. Finally, the FeM is related to the third extraction. At the end, the equivalent to the Fe as structural Fe was obtained: FeS = FeT - FeA - FeD - FeM which is included in other minerals and amorphous phases. To test accuracy, 30 mg of Arizona Test Dust (ATD; ISO 12103-1, A1 Ultrafine Test Dust; Powder Technology Inc.) was subjected to the same extraction procedure in every batch and extraction.

The averaged Fe content of the reference material 1633b was 7.6 ± 0.5 % (certified 7.8%). Furthermore, the average values of the sequential Fe extraction of the ATD reference material were 0.073 ± 0.012, 0.47 ± 0.01, and 0.042 ± 0.002 % for FeA, FeA+FeD and FeM, respectively, while the certified contents are 0.067, 0.48, and 0.047 %, respectively.

3. Results

3.1. Particle size distribution

The PSD and median particle diameter of fully and minimally disturbed samples are key parameters for understanding the cohesion and aggregation state of sediments (González-Romero et al., 2024). We note that in the Mojave Desert some basins are enriched in salts, which can cause some artefacts in the FDPSD. The dissolution of salts during wet dispersion for bulk PSD analysis (<2 mm) can remove aggregating agents. These salt cementation of the crusts might reduce the dust emission potential of the surface.

The average PSDs of crusts across different basins exhibit remarkable similarity, yet disparities between FDPSDs and MDPSDs are pronounced, indicating varying degrees of particle cohesion and aggregation at Cronese, Mesquite, Ivanpah and Coyote lakes. In these locations, FDPSDs feature a dominant mode at 8-10 µm alongside a coarser mode at 100 µm, while MDPSDs are characterised by a dominant coarser mode (Figure 5). In contrast, Soda Lake crusts exhibit similarity between FDPSDs and MDPSDs. Averaged FDPSDs and MDPSDs of aeolian ripples from the Mojave Desert are found to be similar, typically featuring a major size mode between 100-300 µm. However, distinctions arise when analysing specific lakes. Aeolian ripples from Soda, Cronese, and Coyote lakes showcase a dominant coarse mode at 200-300 µm, whereas those from Mesquite Lake show a dominant mode at a finer scale, approximately at 100 µm (Figure 5).

The crusts' mean of all median particle diameters (mean median) in the analysed Mojave Desert dust source sediments reveal a coarser MDPSD compared to FDPSD, with values of 92 and 37 µm, respectively. In contrast, the mean median particle diameter is similar for aeolian ripples (226 and 213 µm, respectively) (Table S1). Analysing specific locations, the mean median particle diameter from the MDPSD of crusts varies, with the finest crust observed at Ivanpah Lake (35 µm) and the coarsest at Mesquite Lake (141 µm). For FDPSD, the finest crust originates from Coyote Lake (8.4 µm), while the coarsest is from Soda Lake (52 µm) (Table S1). Similarly, for aeolian ripples, the mean median particle diameters for both MDPSD and FDPSD are finer at Mesquite Lake (167 and 67 µm, respectively) and coarser at Cronese lakes (264 and 234 µm, respectively) (Table S1). The high degree of particle aggregation observed in crusts, contrasting with the lower aggregation state in ripples, aligns with findings reported for dust-emitting sediments from Morocco by González-Romero et al. (2023).

The mean median particle diameters of crusts collected in the Mojave Desert are similar to those from Morocco described by González-Romero et al. (2023). Specifically, the mean median MDPSD diameter for the Mojave Desert (92 ± 74 µm) closely resembles that of the Morocco Draâ Lower basin (113 ± 79 µm), albeit slightly finer, and is notably coarser than that of Iceland (55 ± 62 µm) (González-Romero et al., 2023, 2024). Furthermore, the finest crust sampled in the Mojave Desert (Ivanpah with 35 µm) is almost twice as coarse as the finest from Morocco (L'Bour with 20 µm). For FDPSD, the Icelandic top sediment surface is the coarsest (56 ± 69 µm), followed by both Morocco and Mojave crusts (37 ± 77 and 37 ± 48 µm, respectively). Additionally, average MDPSD median diameters of aeolian ripples from the Mojave Desert sources samples closely resemble those from Morocco (226 and 221 µm, respectively), while those from Iceland are slightly coarser (280 µm).

Dry sieved size fractions of dust-emitting sediments show the highest percentage of mass in the 250-500 and 80-250 µm fractions, with minimal mass within 500-1000 µm, 1-2 mm and the finer fractions (20-40 and <20 µm) (Figure 6, Table S2). In both cases, the size fractions from 80 to 500 µm accumulated a total of 75 to 90 % of the total mass fraction (Table S2).

Close to the centre of the Soda Lake, where numerous crust samples were collected, before reaching massive crust cementation by evaporite minerals, the FDPSD median diameter reaches very fine sizes (8-15 µm) (Figure S1). In contrast, towards the edges of the basin (closer to the mountains surrounding this endorheic lake), the size markedly increases, ranging from 22 to 87 µm (Figure S1). Similar patterns, yet with coarser sizes, are observed for the MDPSD. As described in previous studies, the fluctuation of the groundwater table in the centre of the basin can lead to a massive precipitation of salts, resulting in the formation of compact crusts (Figure 4) (Reynolds et al., 2007; Nield et al., 2016a; Nield et al., 2016b; Urban et al., 2018) that should effectively reduce dust emission. However, at the edges, where the precipitation of salts is less frequent, and reworking of the crusts by fluctuations in the groundwater table occurs, salty and spongy crusts are formed (Figure 4) (Nield et al., 2016a and Nield et al., 2016b). These spongy crusts, being less compact, are more easily broken by saltating particles, potentially leading to high-salt dust emissions.

The slight particle size segregation, with finer particles accumulating towards the center of the lake, can be attributed to the transport of sediments from the surrounding mountains to the lake's center by runoff waters during rain episodes. Initially, the coarser particles are deposited, followed by the finer particles that remain suspended in the water for a longer duration. Nevertheless, the crusts in the surroundings alluvial fans of the Soda Lake are fine enough (22-87 µm in the edges compared to 8-15 µm in the centre, Figure S1) and surrounded by dunes (availability of saltators for saltation bombardment) to have a high potential dust emission under favourable conditions (Reynolds et al., 2006; Reheis et al., 2009; Urban et al., 2018).

3.2. Mineralogy

Dust-emitting sediments from the Mojave Desert primarily consist of feldspars (41 ± 12 %, including albite/anorthite and microcline), quartz (22 ± 11 %) and clay minerals (18 ± 12 %, such as kaolinite, montmorillonite and illite). Additionally, minor contents of carbonate minerals (6.6 ± 6.6 %), amphibole (pargasite) 4.1 ± 1.5 %, and iron oxides (maghemite/magnetite) (0.77 ± 0.54 %) are observed (Figure 7, Tables 2 and S3). At Soda, Mesquite and Cronese lakes, Na-salts such as halite, thenardite, trona, and burkeite are also present, with an average salt content of 5.0 ± 11 %. Additionally, zeolites (0.77 ± 1.1% to 8.5%) including laumontite and analcime are detected at Soda, Cronese, and Coyote lakes (the southern sites), with the highest content observed at Coyote Lake. High amounts of gypsum are found at Mesquite Lake (15 ± 29 %) (Figure 7, Tables 2 and S3). Moreover, Mesquite Lake crusts exhibit high contents of dolomite and calcite (15 ± 11%) compared to other basins (3.6 ± 2.6% to 7.2%) (Table 2).

The overall mineral composition of the dust-emitting sediments originates primarily from the source rocks prevalent in the region. These include dominant of Mesozoic granitic rocks, as well as pre-Tertiary, Tertiary and Quaternary volcanic rocks, and Pre-Cambrian and Mesozoic metamorphic rocks (Figure 1). In the northern, northeastern, and eastern areas of Mesquite Lake, an important limestone and dolostone massif from the Palaeozoic era contributes notably to the high content of calcite and

437 dolomite in the sediments of this lake (Figure 1). Zeolite content in the sediments may be attributed
438 to the weathering of volcanic outcrops in the region or to precipitation in alkaline lakes. This diverse
439 bedrock mineralogy results in a wide variety of minerals in the dust-emitting sediments. The form of
440 iron oxide detected in the samples, identified via XRD, is maghemite. However, distinguishing between
441 maghemite and magnetite using XRD is challenging (Vandenberghe et al., 2000), and magnetite has
442 been found to be ubiquitous in Mojave dust (Reheis et al., 2009; Reynolds et al., 2006). Therefore, we
443 refer to maghemite/magnetite to account for the potential presence of both minerals in the samples.
444 In comparison to aeolian ripples, the average composition of the crusts shows enrichment in clay
445 minerals (24 ± 11 versus 7.8 ± 2.3 % in crust and ripples, respectively), carbonates (6.6 ± 6.6 versus 1.1
446 ± 2.2 %), Na-salts (7.3 ± 13 versus 1.1 ± 3.7 %), zeolites (1.2 ± 1.9 versus 0.12 ± 0.52 %) and
447 maghemite/magnetite (0.92 ± 0.59 versus 0.49 ± 0.28 %), while being depleted in quartz (16 ± 7.2
448 versus 32 ± 9.5 %), feldspars (37 ± 9.7 versus 48 ± 13 %) and gypsum (3.1 ± 14 versus 4.7 ± 20 %), and
449 showing a similar amphibole content (4.1 ± 1.5 versus 4.1 ± 1.6 %) (Figure 7, Tables 2 and S3). These
450 mineral enrichment and depletion trends in crusts are observed in all the playa lakes, except for
451 Mesquite Lake, which is discussed below.

452 In Soda Lake, the concentration of Na-salts in crusts increases towards the inner part of the lake,
453 ranging from 5-10 % at the margins to 45-50 % in the centre, where compact and fully salt-cemented
454 crusts form. This phenomenon is illustrated in Figure 8, which presents a geological and mineralogical
455 cross-section of Soda Lake. In addition to the water transport to this central part of the basin during
456 the rain episodes, groundwater discharge from the Zzyzx mountains occurs. There, the groundwater
457 table is close to the surface, and its interaction with the surface causes the massive mobilisation of
458 Na-salts that consolidate the crusts (Figure 4) (Nield et al., 2016b). Cycles of precipitation and
459 dissolution of the salts yield salty spongy crusts (Figure 4) at the edges of these massive crusts, with
460 higher dust emission potential in the degraded salty crusts (Nield et al., 2016a). The very high content
461 of Na-salts content in Soda Lake is attributed to the continuous high Na-S-Cl groundwater interaction
462 in the vicinity of Zzyzx, defining Soda Lake as a wet playa lake according to Reynolds et al. (2009) and
463 Urban et al. (2018). On the other hand, Cronese, Coyote, and Ivanpah are categorised as dry lakes.

464 Mesquite Lake features extensive gypsum deposits at the surface, which are a major component of
465 both dunes and crusts. A small gypsum mine operates in Mesquite Lake. The gypsum content in crusts
466 is notably higher at the center (80%) compared to the margins (3-11%). In contrast, the contents of
467 Na-salts and carbonates are greater at the margins (30% and 12-18%, respectively) than at the center
468 (7.5-14% and <0.1-6.9%, respectively). Aeolian ripples at the center of Mesquite Lake exhibit a very
469 high gypsum content, whereas at the margins, these ripples contain higher amounts of quartz,
470 feldspars, and clays than at the center. Despite the presence of the disturbed mine area, most large
471 dust events at Mesquite Lake have been observed to originate from natural (undisturbed) playa
472 surfaces near the margins (Reynolds R., personal communication).

473 Amphiboles in the Mojave Desert, sourced from metamorphic rocks in the area, are homogeneous
474 and can serve as a marker for emitted desert dust in the region. Comparing mineralogy from Mojave
475 Desert crusts to Moroccan surface samples (González-Romero et al., 2023), the former are largely
476 enriched in feldspars, clay minerals, Na-salts, and gypsum, and depleted in quartz and carbonates,
477 with trace proportions of amphibole, zeolites, and maghemite/magnetite. Ripples in the Mojave
478 Desert are depleted in quartz and carbonates, enriched in feldspars, clay minerals, Na-salts, and
479 gypsum, with traces of amphibole, maghemite/magnetite, and zeolites compared to Moroccan

480 ripples. The mineralogy of the Mojave Desert is markedly different from that of Iceland, due to
481 differences in bedrock geology, although both contain feldspars, zeolites, and maghemite/magnetite
482 (González-Romero et al., 2024).

483 Particle aggregation of the dust-emitting sediments from the Mojave Desert samples is similar to those
484 described by González-Romero et al. (2023) for Moroccan samples, likely due to the presence of clays,
485 Na-salts and precipitated carbonates. This aggregation inhibits aerodynamic entrainment and dust
486 emission should be primarily controlled by saltation bombardment (Shao et al., 1993). According to
487 the XRD analysis, the occurrence of crystalline Fe oxides is limited to maghemite/magnetite in contrast
488 to the hematite/goethite content found in Moroccan crusts (González-Romero et al., 2023). However,
489 due to the XRD low precision on the detection of low contents of minerals such as hematite and
490 goethite, their presence in the samples cannot be ruled out. In fact, both the EMIT standard products
491 (Figure 3), and the Fe mode of occurrence analysis discussed in the next section suggest the presence
492 of hematite and goethite.

493 The EMIT standard products (Figure 3) indicate the presence of phyllosilicates such as kaolinite,
494 smectite, montmorillonite, and illite, broadly consistent with our results. Specifically, around Mesquite
495 Lake, where elevated levels of gypsum and carbonates were detected, the EMIT results corroborate
496 the significance of these minerals in the same vicinity. Similarly, in Coyote, Ivanpah, and Cronese Lakes,
497 there is agreement regarding the prevalence of illite and muscovite as the major clay minerals,
498 alongside kaolinite. However, discrepancies arise in Soda Lake, where EMIT identifies a dominant
499 presence of montmorillonite, contrasting with our XRD results indicating a predominance of illite,
500 muscovite, and kaolinite. While Tetracorder identified predominant montmorillonite, illite, muscovite
501 and kaolinite could be on the order of 30% of the montmorillonite abundance and not show in the
502 EMIT spectra without a more sophisticated non-linear radiative transfer model to find the relative
503 abundances of these two minerals. This is due to the relative absorption strengths of the spectral
504 features of these minerals relative to those in montmorillonite. While our XRD analyses highlight the
505 presence of maghemite/magnetite, these minerals do not present clear absorbing features in the
506 spectral range of the EMIT instrument and are not considered within the 10 EMIT standard minerals.
507 In contrast to the XRD results, EMIT highlights the significant presence of goethite in the northern
508 sources (Mesquite and Ivanpah Lakes). Conversely, in the southern sources (Soda, Cronese, and
509 Coyote Lakes), EMIT highlights a major mixture of Fe2+ and Fe3+ species. The limited precision of XRD
510 for low proportions of Fe oxides, underscores the need for complementary techniques and analyses
511 to bolster our findings.

512 The mineralogical composition of the dry size-segregated fractions of the dust-emitting sediments is
513 outlined in Table S4. The findings indicate that there is no significant size enrichment process in crusts;
514 rather, there exists a relatively uniform distribution of quartz, feldspars, zeolites, and Fe oxides across
515 all size fractions (Figure 6). A slight, albeit not significant, enrichment of carbonates and clays is
516 observed, along with a slight depletion of Na-salts and gypsum in the finer fractions (<20 μm).
517 Additionally, pargasite shows a slight enrichment in the 40-80 μm fraction. In contrast, for aeolian
518 ripples, quartz exhibits significant enrichment in the coarser fraction (250-500 μm) and depletion in
519 the finer ones (<80 μm). Regarding carbonates, clays, and Fe oxides, there is an enrichment towards
520 the finer fractions (<20 μm), while the content of feldspars remains relatively homogeneous. Pargasite
521 content increases in the 40-80 μm fraction, and Na-salts and gypsum are either not detected or
522 present in trace amounts (Figure 6). The notable disparity in the enrichment factor between crusts

523 and aeolian ripples is partly attributed to the reduced amount of sand in crusts and the differing
524 cohesion states: crusts exhibit high cohesion, resulting in a homogenised mineralogy across size
525 fractions (as aggregates form a homogeneous concretion of minerals), while aeolian ripples display
526 lower or negligible aggregation, leading to a slightly more heterogeneous mineralogy across size
527 fractions compared to crusts.

3.3. Mode of occurrence of Fe

529 The average content of FeT in the crusts is 3.0 ± 1.3 wt %, while for aeolian ripples is 1.9 ± 1.1 wt %.
530 Among these crusts, 1.8 ± 0.92 % of the FeT occurs as FeA, 17 ± 7.2 % as FeD, 2.1 ± 1.2 as FeM and 79
531 ± 8.5 % as FeS (Tables 3 and S5). Aeolian ripples have very similar contents and modes of occurrence
532 of Fe in the analysed samples of the Mojave Desert.

533 Among the crusts, Ivanpah has the highest FeT content at 4.9 %, followed by Cronese and Coyote lakes
534 (3.7 ± 1.2 % and 3.5 %, respectively), with Soda Lake showing a similar content (3.1 ± 1.2 %). Mesquite
535 has the lowest FeT (1.6 ± 0.53 %), probably due to dilution of detrital Fe-bearing minerals with salts
536 and gypsum. FeS is the dominant mode of occurrence in most lakes, ranging from 68 % (1 sample) at
537 Ivanpah, to 74 ± 3.5 and 74 ± 13 % at Mesquite and Cronese, and to 83 ± 2.8 and 82 % at Soda and
538 Coyote lakes. The FeD is higher at Ivanpah (29 %), Cronese Lakes (21 ± 11 %) and Mesquite Lake (20 ±
539 2.7 %) than at Soda and Coyote lakes (14 ± 2.5 and 14 %). FeM is higher at Mesquite Lake (3.7 ± 1.2
540 %), followed by Cronese and Coyote lakes (2.3 ± 1.1 and 2.4 %), and Soda (1.5 ± 0.49 %) and Ivanpah
541 Lakes (0.82 %). Finally, FeA is higher at Cronese Lake (2.4 ± 0.99 %), compared to Coyote, Mesquite,
542 Soda and Ivanpah lakes (1.8, 1.8 ± 0.93, 1.5 ± 0.81 and 1.4 %) (Tables 3 and S5). Crusts are enriched in
543 FeT, FeD and FeA compared to ripples, while ripples are enriched in FeM and FeS (Tables 3 and S5).

544 Overall, the bulk Fe content in crusts is driven by structural Fe from clays and amphiboles (as deduced
545 from the high correlation shown in Figure 9a), followed by small proportions of hematite and goethite
546 (not detected by XRD), which are clearly higher at the northern lakes Ivanpah and Mesquite lakes
547 (consistent with the highlighted presence of goethite in the EMIT standard products), probably due to
548 the Precambrian and Cambrian metamorphic rocks that supply sediments. Furthermore, the easily
549 exchangeable Fe is also driven by clay minerals (Figure 9b).

550 Compared to crusts in other arid regions analysed by González-Romero et al. (2023, 2024), the
551 analysed Mojave Desert crusts have similar FeT content than Moroccan crusts but are much lower
552 than the Iceland top sediments (loose surface sediments in Iceland according to González-Romero et
553 al. (2024)) (3.0 ± 1.3, 3.6 ± 0.71 and 9.5 ± 0.39 %, for Mojave, Morocco, and Iceland respectively). The
554 proportion of FeS in FeT is similar to the Icelandic sediments but higher than in Moroccan samples (79
555 ± 8.5 and 79 ± 6.5 %, and 67 ± 2.4, respectively). The proportion of FeM is clearly lower than that of
556 Iceland, but higher than that of Morocco (2.1 ± 1.2 and 16 ± 5.4 %, for Mojave and Iceland; Morocco
557 proportion is negligible). The FeD proportion is intermediate between Morocco and Iceland (17 ± 7.2,
558 31 ± 2.3, 3.5 ± 1.5 %, respectively), while the FeA proportion is similar to both Morocco and Iceland
559 crusts (1.8 ± 0.92, 1.3 ± 0.39 and 1.9 ± 0.55 %, respectively) (Figure 10).

4. Discussion and conclusions

561 The playa lakes sampled within the Mojave Desert can serve as significant dust-emitting sources in the
562 region. Descriptions provided by Urban et al. (2018) and satellite imagery (Figure 2) confirm the

563 presence of desert dust emissions originated from these areas. The lithology, geological/tectonic
564 evolution, and past and current climate conditions collectively contribute to the formation of these
565 dust sources in the Mojave Desert.

566 Dust-emitting sediments in this region predominantly stem from substratum rocks, comprising mainly
567 granitic and volcanic formations, along with metamorphic Pre-Cambrian, Cambrian, Paleozoic, and
568 Mesozoic rocks. Endorheic basins, shaped by faulting during the Tertiary-Quaternary period,
569 accumulated fine sediments through erosion, transportation, and deposition processes. Wetter
570 conditions prevailing during the Pleistocene epoch led to the formation of deep lakes within the
571 basins, which gradually desiccated as the climate evolved. These arid conditions rendered the playa
572 lakes susceptible to dust emission under specific atmospheric conditions. Notably, a particle size
573 segregation is observed, transitioning from coarser sediments in the proximal alluvial areas towards
574 finer particle crusts within the central regions of the lakes. In the playa lakes, finer sediments
575 accumulate towards the centre of the lakes due to flood events inundating the central areas and
576 ponding, which facilitates the deposition of coarser particles followed by top finer sediment sizes.

577 As represented in the conceptual model depicted in Figure 11, the finer dust particle size distributions
578 range from 8.4 to 99 μm inside Soda Lake and 46 to 111 μm outside Soda Lake, underscoring this
579 sedimentation process. Comparisons with conceptual models proposed for other regions, such as
580 those by González-Romero et al. (2023, 2024) for locations in Morocco and Iceland, reveal a similar
581 transport fractionation phenomenon occurring in the Mojave Desert. These crusts, observed within
582 Soda Lake, show enrichment in clay minerals, carbonate minerals, salts, and iron oxides, while
583 experiencing depletion in coarser constituents such as feldspars and quartz.

584 In the Mojave Desert, there are two distinct types of playa lakes, characterised as wet and dry,
585 depending on the regime of the groundwater table and its relationship with the surface, as described
586 by Reynolds et al. (2007 and 2009), Buck et al. (2011), Nield et al. (2016a and b), Urban et al. (2018)
587 and Goudie (2018). Understanding the groundwater table regime is fundamental in this region due to
588 its profound relation on the porosity of the crust and its consequential impact on mineralogy, including
589 the precipitation and enrichment of salts (Figure 11). This dynamic contrasts sharply with other
590 conceptual models, where the relationship between crust formation and the groundwater table is
591 either minimal or absent entirely. For instance, there is no or little relation between crusts and
592 groundwater table in Morocco, and in Iceland, where the water regime is largely influenced by
593 floodings from glaciers (González-Romero et al., 2023, 2024). In wet playa lakes like Soda Lake, the
594 presence of salty crusts, whether massive or spongy, is significantly pronounced. Conversely, in dry
595 playa lakes such as Ivanpah, Coyote, and Cronese, the relationship of salt crusts is notably less
596 prominent as the proportion of Na-salts is lower (see Figure 11).

597 At Soda Lake, a hard crust, measuring up to 0.5 meters in thickness (Figure 3), forms through the
598 extensive precipitation of Na-salts, particularly near the Zzyzx area, where a relatively constant
599 mobilisation of salts is due to the water table evaporation or vapour discharge from deeper parts of
600 the sediment towards the surface (Nield et al., 2015, 2016a and b). Along the edges of this massive
601 crusty area, the frequent oscillation of the water table may result in the precipitation and dissolution
602 of salts in lower quantities compared to the centre, leading to the formation of weaker crusts
603 characterised by high porosity. These porous crusts may contribute to an increased dust emission rate
604 compared to the hard salt crusts found in the centre. Dry lakes such as Ivanpah, Cronese, and Coyote

605 do not exhibit the formation of spongy crusts due to the low concentrations of salts. In wet playas,
606 strong dust emission may happen when very strong winds rip off thin crusts exposing the fine-grained
607 sediment beneath including lithogenic and salt mineral particles (Rich Reynolds, personal
608 communication).

609 Particle aggregation facilitated by diagenetic salts and carbonate minerals is prevalent in the dust-
610 emitting sediments sampled in the Mojave Desert, akin to the equivalent sediments found in the
611 Moroccan Sahara. The average grain size of the crusts from both regions is similar, with MDPSD values
612 of 113 ± 79 µm for Morocco and 92 ± 74 µm for the Mojave Desert, and FDPSD values of 37 ± 77 µm
613 and 37 ± 48 µm, respectively. These patterns contrast with the lower aggregation state and finer
614 MDPSD observed in Icelandic dust (55 ± 62 µm) (Table 4).

615 In terms of mineralogy, crusts from the Mojave Desert are enriched in feldspars, clay minerals, Na-
616 salts, and gypsum, whereas crusts from the Moroccan Sahara are enriched in quartz and carbonates
617 (Table 4). The mineralogy of Icelandic top sediments (loose surface sediments in Iceland according to
618 González-Romero et al. (2024)) differs due to their volcanic origin; however, both the Mojave Desert
619 crusts and Icelandic top sediments contain similar amounts of zeolites. Salt enrichment in the crusts
620 is primarily attributed to interactions with the groundwater table as shown in previous studies (Nield
621 et al. (2016a and b), Urban et al. (2018) and Goudie (2018) (Figure 11).

622 The total iron content (FeT) remains consistent throughout the samples collected in the Mojave
623 Desert, with slightly higher levels observed in the Ivanpah crust, albeit diluted by the high salt content
624 in the wet playa lake crusts or the elevated gypsum content in the Mesquite Lake. While the total Fe
625 content is comparable between the Mojave Desert and Moroccan Sahara crusts (3.0 and 3.6 wt %,
626 respectively), it is substantially lower than in Icelandic top sediments (9.3 wt %). Exchangeable Fe
627 proportions in FeT are similar among the three environments. The proportion of Fe from hematite and
628 goethite in Mojave Desert crusts fall between those of Moroccan Sahara crusts and Icelandic top
629 sediments (17, 31, and 0.5 wt %, respectively). The proportion of maghemite/magnetite in Mojave
630 Desert crusts is much lower compared to Icelandic top sediments (2.1 and 15 %, respectively). Finally,
631 the proportion of structural Fe in the samples is similar across the three environments.

632 In conclusion, the dust-emitting sediments collected from the Mojave Desert exhibit distinct
633 signatures in mineralogy and modes of occurrence of Fe compared to those from the Moroccan
634 Sahara, despite similar particle sizes. These differences can influence emitted dust properties, and
635 associated impacts. Similarities in fully disturbed and minimally disturbed particle size distributions
636 support comparable dust emission mechanisms, with saltation bombardment playing a prominent
637 role.

638 **Code availability.** The Tetracorder code used in this paper is provided by Clark (2023,
639 https://github.com/PSI-edu/spectroscopy-tetracorder).

640 **Data availability.** Data used in this paper are given in the main paper itself and in the Supplement. If
641 needed, data are also available upon request by emailing the authors.

642 **Author contribution.** Sample permits were obtained by BLE, RG and AK. The samples were collected
643 by CPG-P, AGR, AK, RG and XQ and analysed by AGR, MHC and NM. EMIT mineralogy maps we
644 produced by RG, PB and RC. PG provided the FoO map. AGR analysed the data and wrote of the original

draft manuscript supervised by CPG-P and XQ. CPG-P and XQ re-edited the manuscript and all authors contributed to data discussion, reviewing and manuscript finalization.

Competing interests. At least one of the (co-)authors is a member of the editorial board of Atmospheric chemistry and Physics.

Acknowledgements

We thank Richard Reynolds and another anonymous reviewer for the helpful comments and suggestions to improve the manuscript.

The field campaign and its associated research, including this work, was funded by the European Research Council under the Horizon 2020 research and innovation programme through the ERC Consolidator Grant FRAGMENT (grant agreement No. 773051) and the AXA Research Fund through the AXA Chair on Sand and Dust Storms at BSC. CGF was supported by a PhD fellowship from the Agència de Gestió d'Ajuts Universitaris i de Recerca (AGAUR) grant 2020_FI B 00678. KK was funded by the Deutsche Forschungsgemeinschaft (DFG, German Research Foundation) – 264907654; 416816480. MK has received funding through the Helmholtz Association's Initiative and Networking Fund (grant agreement no. VH-NG-1533). We acknowledge the EMIT project, which is supported by the NASA Earth Venture Instrument program, under the Earth Science Division of the Science Mission Directorate. We are grateful to Claire Blaske and Sahil Azad for assistance sampling in the Mojave National Preserve. Samples within the preserve were collected under permit MOJA-2022-SCI-0034. We thank Rose Pettiette at the BLM office in Needles, CA, for advice and allowing sampling on BLM land. We thank Jason Wallace and Anne Kelly from CSU Desert Studies Center at Zzyzx for their support during the campaign. BLE, RG, and AMK thank the Resnick Sustainability Institute at Caltech for partial support. Without all of them, the sampling campaign would not have been successfully feasible.

5. References

Alfaro, S. C., Gaudichet, A., Gomes, L., & Maillé, M. (1997). Modeling the size distribution of a soil aerosol produced by sandblasting. Journal of Geophysical Research: Atmospheres, 102(D10), 11239-11249.

Arnalds, Ó., Olafsson, H. and Dagsson-Waldhauserova, P.: Quantification of iron-rich volcanogenic dust emissions and deposition over the ocean from Icelandic dust sources, Biogeosciences, 11, 6623-6632. https://doi.org/10.5194/bg-11-6623-2014, 2014.

Atkinson, J. D., Murray, B. J., Woodhouse, M. T., Whale, T. F., Baustian, K. J., Carslaw, K. S., ... & Malkin, T. L.: The importance of feldspar for ice nucleation by mineral dust in mixed-phase clouds. Nature, 498(7454), 355-358, 2013.

Baddock, M. C., Ginoux, P., Bullard, J. E., & Gill, T. E. (2016). Do MODIS-defined dust sources have a geomorphological signature?. Geophysical Research Letters, 43(6), 2606-2613.

Baldo, C., Formenti, P., Nowak, S., Chevaillier, S., Cazaunau, M., Pangui, E., Di Baggio, C., Doussin, J.F., Ignatyev, K., Dagsson-Waldhauserova, P., Arnalds, O., MacKenzie, A.R., Shi, Z.: Distinct chemical and mineralogical composition of Icelandic dust compared to Northern African and Asian dust. Atmospheric Chemistry and Physics, 20, 13521-13539, 2020.

683 Bauer, S. E., & Koch, D.: Impact of heterogeneous sulfate formation at mineral dust surfaces on aerosol
684   loads and radiative forcing in the Goddard Institute for Space Studies general circulation
685   model. Journal of Geophysical Research: Atmospheres, 110(D17), 2005.

686 Beaudoing, H., Rodell, M., & NASA/GSFC/HSL: GLDAS Noah Land Surface Model L4 monthly 0.25 x 0.25
687   degree, Version 2.1 [dataset]. NASA Goddard Earth Sciences Data and Information Services
688   Center. 2020. https://doi.org/10.5067/SXAVCZFAQLNO.

689 Buck, B.J., King, J. and Etyemezian, V., 2011. Effects of salt mineralogy on dust emissions, Salton Sea,
690   California. Soil Science Society of America Journal, 75(5), pp.1971-1985.

691 Bullard, J. E., Harrison, S. P., Baddock, M. C., Drake, N., Gill, T. E., McTainsh, G., & Sun, Y. (2011).
692   Preferential dust sources: A geomorphological classification designed for use in global dust-
693   cycle models. Journal of Geophysical Research: Earth Surface, 116(F4).

694 Chatziparaschos, M., Daskalakis, N., Myriokefalitakis, S., Kalivitis, N., Nenes, A., Gonçalves Ageitos, M.,
695   Costa-Surós, M., Pérez García-Pando, C., Zanoli, M., Vrekoussis, M. & Kanakidou, M.: Role of K-
696   feldspar and quartz in global ice nucleation by mineral dust in mixed-phase clouds.
697   Atmospheric Chemistry and Physics, 23(3), 1785-1801, 2023.Cheary, R.W., Coelho, A.: A
698   fundamental parameters approach to X-ray line profile fitting. Journal of Applied
699   Crystallography 25, 109–121, 1992.

700 Claquin, T., Schulz, M., & Balkanski, Y. J. (1999). Modeling the mineralogy of atmospheric dust sources.
701   Journal of Geophysical Research: Atmospheres, 104(D18), 22243-22256.

702 Clark, Roger N., 2024, PSI-edu/spectroscopy-tetracorder: Tetracorder 5.27 with expert systems to
703   5.27e + specpr, spectral libraries, and radiative transfer models (v5.27.0). Zenodo.
704   https://doi.org/10.5281/zenodo.11204505

705 Clark, R. N., G. A. Swayze, K. E. Livo, P. Brodrick, E. Noe Dobrea, S. Vijayarangan, R. O. Green, D.
706   Wettergreen, A. Candela, A. Hendrix, C. P. Garcia-Pando, N. Pearson, M. D. Lane, A. Gonzalez-
707   Romero, X. Querol, and the EMIT and TREX teams, 2024. Imaging spectroscopy: Earth and
708   planetary remote sensing with the PSI Tetracorder and expert systems: from Rovers to EMIT
709   and Beyond Planetary Science Journal in review. Crumeyrolle, S., Gomes, L., Tulet, P., Matsuki,
710   A., Schwarzenboeck, A., and Crahan, K.: Increase of the aerosol hygroscopicity by cloud
711   processing in a mesoscale convective system: a case study from the AMMA campaign, Atmos.
712   Chem. Phys., 8, 6907–6924, https://doi.org/10.5194/acp-8-6907-2008, 2008.

713 De la Torre, A.G., Bruque, S., Aranda, M.A.G.: Rietveld quantitative amorphous content analysis.
714   Journal of Applied Crystallography, 34:196-202, 2001.

715 De Longueville, F., Hountondji Y.C., Henry S., Ozer P.: What do we know about effects of desert dust
716   on air quality and human health in West Africa compared to other regions?. Sci. Total Environ.,
717   409, 1–8, 2010.

718 Dibblee T.W.: Areal geology of the western mojave desert California. Geological Survey Professional
719   paper, 522, https://doi.org/10.3133/pp522, 1967.

720 Di Biagio, C., Formenti, P., Balkanski, Y., Caponi, L., Cazaunau, M., Pangui, E., Journet, E., Nowak, S.,
721   Andreae, M.O., Kandler, K., Saeed, T., Piketh, S., Seibert, D., Williams, E., Doussin, J.F.: Complex
722   refractive indices and single-scattering albedo of global dust aerosols in the shortwave
723   spectrum and relationship to size and iron content. Atmos. Chem. Phys., 19, 15503-15531.
724   https://doi.org/10.5194/acp-19-15503-2019, 2019.

725 Eghbal, M.K., Southard, R.J.: Mineralogy of Aridisols on Dissected Alluvial Fans, Western Mojave
726   Desert, California. Soil Science Society of America Journal, 57, pp. 538-544, 1993.

Engelbrecht, J.P., Moosmüller, H., Pincock, S., Jayanty, R.K.M., Lersch, T., Casuccio, G.: Technical note: Mineralogical, chemical, morphological, and optical interrelationships of mineral dust re-suspensions. Atmos. Chem. Phys., 16, 10809-10830. https://doi.org/10.5194/acp-16-10809-2016, 2016.

Floyd, K. W., & Gill, T. E. (2011). The association of land cover with aeolian sediment production at Jornada Basin, New Mexico, USA. Aeolian Research, 3(1), 55-66.

Formenti, P., Caquineau, S., Chevaillier, S., Klaver, A., Desboeufs, K., Rajot, J.L., Belin, S., Briois, V.: Dominance of goethite over hematite in iron oxides of mineral dust from Western Africa: Quantitative partitioning by X-ray absorption spectroscopy. J. Geophys. Res. Atmos., 119, 12740-12754, https://doi.org/10.1002/2014jd021668, 2014.

Frank, T.D., Di Girolamo, L., Geegan, S.: The spatial and temporal variability of aerosol optical depths in the Mojave desert of southern California. Remote Sensing of Environment, 107, 1-2, 54-64, https://doi.org/10.1016/j.rse.2006.06.024, 2007.

Ginoux, P., Chin, M., Tegen, I., Prospero, J. M., Holben, B., Dubovik, O., & Lin, S. J. (2001). Sources and distributions of dust aerosols simulated with the GOCART model. Journal of Geophysical Research: Atmospheres, 106(D17), 20255-20273.

Ginoux, P., Prospero, J.M., Gill, T.E., Hsu, N.C., Zhao, M.: Global-scale attribution of anthropogenic and natural dust sources and their emission rates based on MODIS Deep Blue aerosol products. Rev. Geophys., 50, RG3005, doi:10.1029/2012RG000388, 2012.

Goldstein, H.L., Breit, G.N., & Reynolds, R.L.: Controls on the chemical composition of saline surface crusts and emitted dust from a wet playa in the Mojave Desert (USA). Journal of Arid Environments, 140, 50-66, 2017.

González-Flórez, C., Klose, M., Alastuey, A., Dupont, S., Escribano, J., Etyemezian, V., ... & Pérez García-Pando, C. (2022). Insights into the size-resolved dust emission from field measurements in the Moroccan Sahara. Atmospheric Chemistry and Physics Discussions, 2022, 1-65.

González-Romero, A., González-Florez, C., Panta, A., Yus-Díez, J., Reche, C., Córdoba, P., Moreno, N., Alastuey, A., Kandler, K., Klose, M., Baldo, C., Clark, R.N., Shi, Z.B., Querol, X., Pérez García-Pando, C.: Variability in grain size, mineralogy, and mode of occurence of Fe in surface sediments of preferential dust-source inland drainage basins: The case of the Lower Drâa Valley, S Morocco. Atmos. Chem. Phys., 23, 15815–15834, https://doi.org/10.5194/acp-23-15815-2023, 2023.

González-Romero, A., González-Florez, C., Panta, A., Yus-Díez, J., Córdoba, P., Alastuey, A., Moreno, N., Kandler, K., Klose, M., Clark, R.N., Ehlmann, B.L., Greenberger, R., Keebler, A.M., Brodick, P., Green, R., Querol, X., Pérez García-Pando, C.: Probing Iceland's Dust-Emitting Sediments: Particle Size Distribution, Mineralogy, Cohesion, Fe Mode of Occurrence, and Reflectance Spectra Signatures. Atmospheric Chemistry and Physics. EGUSPHERE [Preprint], 2024.

Goudie, A.: Dust storms and ephemeral lakes. Desert, 23(1), 153-164, 2018.

Goudie, A.S. & Middleton, N.J.: Desert dust in the global system. Springer, Heidelberg. ISBN 978-786 3-540-32355-6, 288 pp, 2006.

Green R.O., Mahowald N., Ung C., Thompson D.R., Bator L., Bennet M., Zan J.: The earth surface mineral dust source investigation: an earth science imaging spectroscopy mission. In: IEEE Aerospace Conference Proceedings. IEEE Computer Society. https://doi.org/10.1109/AERO47225.2020.9172731. 2020.

Harrison, A. D., Lever, K., Sanchez-Marroquin, A., Holden, M. A., Whale, T. F., Tarn, M. D., ... & Murray, B. J.: The ice-nucleating ability of quartz immersed in water and its atmospheric importance compared to K-feldspar. Atmospheric Chemistry and Physics, 19(17), 11343-11361, 2019.

Hettiarachchi, E., Reynolds, R. L., Goldstein, H. L., Moskowitz, B., & Rubasinghege, G. Bioavailable iron production in airborne mineral dust: Controls by chemical composition and solar flux. Atmospheric environment, 205, 90-102, 2019.

Hettiarachchi, E., Ivanov, S., Kieft, T., Goldstein, H. L., Moskowitz, B. M., Reynolds, R. L., & Rubasinghege, G. Atmospheric processing of iron-bearing mineral dust aerosol and its effect on growth of a marine diatom, Cyclotella meneghiniana. Environmental Science & Technology, 55(2), 871-881, 2020.

Honke, J.S., Pigati, J.S., Wilson, J., Bright, J., Goldstein, H.L., Skipp, G.L., Reheis, M.C., Havens, J.C.: Late Quaternary paleohydrology of desert wetlands and pluvial lakes in the Soda Lake basin, central Mojave Desert, California (USA). Quat. Sci. Rev., 216, pp. 89-106, 10.1016/j.quascirev.2019.05.021, 2019.

Ibáñez, J., Font, O., Moreno, N., Elvira, J.J., Alvarez, S., Querol, X.: Quantitative Rietveld analysis of the crystalline and amorphous phases in coal fly ashes. Fuel, 105: 314-317, 2013.

Jennings, C.W., Burnett, J.L., and Troxel, B.W.: Geologic map of California: Trona sheet. California Division of Mines and Geology, Geologic Atlas of California, GAM-23, 1:250.000, 1962.

Jickells, T. D., An, Z. S., Andersen, K. K., Baker, A. R., Bergametti, G., Brooks, N., ... & Torres, R.: Global iron connections between desert dust, ocean biogeochemistry, and climate. science, 308(5718), 67-71, 2005.

Journet, E., Balkanski, Y., & Harrison, S. P. (2014). A new data set of soil mineralogy for dust-cycle modeling. Atmospheric Chemistry and Physics, 14(8), 3801-3816.

Karanasiou, A., Moreno, N., Moreno, T., Viana, M., de Leeuw, F., Querol, X.: Health effects from Sahara dust episodes in Europe: Literature review and research gaps. Environ. Int. 47, 107–14, 2012.

Kok, J.F., Adebiyi, A.A., Albani, S., Balkanski, Y., Checa-Garcia, R., Chin, M., Colarco, P.R., Hamilton, D.S., Huang, Y., Ito, A., Klose, M., Li, L., Mahowald, N.M., Miller, R.L., Obiso, V., Pérez García-Pando, C., Rocha-Lima, A., Wan, J.S.: Contribution of the world's main dust source regions to the global cycle of desert dust, Atmos. Chem. Phys., 21, 8169–8193, https://doi.org/10.5194/acp-21-8169-2021, 2021.

Laurent, B., Marticorena, B., Bergametti, G., Léon, J.F., Mahowald, N.M.: Modeling Mineral Dust Emissions from the Sahara Desert Using New Surface Properties and Soil Database J. Geophys. Res., 113, D14218, 2008.

Li, L., Mahowald, N. M., Miller, R. L., Pérez García-Pando, C., Klose, M., Hamilton, D. S., ... & Thompson, D. R. (2021). Quantifying the range of the dust direct radiative effect due to source mineralogy uncertainty. Atmospheric chemistry and physics, 21(5), 3973-4005.

Machiels, L., Mertens, G., Elsen, J.: Rietveld Refinement strategy for Quantitative Phase analysis of Partially Amorphous zeolitized tuffaceous. GEOLOGICA BELGICA 13,3, 183-196, 2010.

Madsen, I.C., Scarlett, N.V.Y., Cranswick, L.M.D., Lwin, T.: Outcomes of the international union of crystallography commission on powder diffraction round robin on quantitative phase analysis: Samples 1a to 1h. J. Appl. Crystallogr., 34, pp. 409-426, 2001.

Mahowald, N.M., Baker, A.R., Bergametti, G., Brooks, N., Duce, R.A., Jickells, T.D., Kubilay, N., Prospero, J.M., Tegen, I.: Atmospheric global dust cycle and iron inputs to the ocean, Global Biogeochem. Cy., 19(4), GB4025, doi:10.1029/2004GB002402, 2005.

814 Matsui, H., Yamane, M., Tonami, T., Nagami, T., Watanabe, K., Kishi, R., Kitagawa, Y., Nakano, M.:
815   Theoretical study on gigantic effect of external static electric field application on nonlinear
816   optical properties of 1,2,3,5-dithiadiazolyl π-radical dimer. Mater. Chem. Front., 2, 785– 790,
817   DOI: 10.1039/C7QM00549K, 2018.

818 Miller, D.M., Menges, C.M., and Lidke, D.J.: Generalized surficial geologic map of the Fort Irwin area,
819   San Bernardino County, California, U.S. Geological Survey, Open-File Report OF-2013-1024-B,
820   1:100.000, 2014.

821 Miller, D.M., Dudash, S.L., & McGeehin, J.P.: Paleoclimate record for Lake Coyote, California, and the
822   Last Glacial Maximum and deglacial paleohydrology (25 to 14 cal ka) of the Mojave River. S.W.
823   Starratt, M.R. Rosen (Eds.), From Saline to Freshwater: The Diversity of Western Lakes in Space
824   and Time: Geologic Society of America Special Paper 536, pp. 1-20, 2018.

825 Nield, J.M., Bryant, R.G., Wiggs, G.F., King, J., Thomas, D.S., Eckardt, F.D., and Washington, R. The
826   dynamism of salt crust patterns on playas. Geology, 43(1), pp.31-34, 2015.

827 Nield, J.M., Neuman, C.M., O'Brien, P., Bryant, R.G., and Wiggs, G.F. Evaporative sodium salt crust
828   development and its wind tunnel derived transport dynamics under variable climatic
829   conditions. Aeolian Research, 23, pp.51-62, 2016.

830 Nield, J.M., Wiggs, G.F., King, J., Bryant, R.G., Eckardt, F.D., Thomas, D.S. and Washington, R. Climate–
831   surface–pore-water interactions on a salt crusted playa: implications for crust pattern and
832   surface roughness development measured using terrestrial laser scanning. Earth Surface
833   Processes and Landforms, 41(6), pp.738-753, 2016.

834 Obiso, V., Gonçalves Ageitos, M., Pérez García-Pando, C., Perlwitz, J. P., Schuster, G. L., Bauer, S. E., …
835   & Miller, R. L. (2024). Observationally constrained regional variations of shortwave absorption
836   by iron oxides emphasize the cooling effect of dust. Atmospheric Chemistry and Physics, 24(9),
837   5337-5367.

838 Panta, A., Kandler, K., Alastuey, A., González-Flórez, C., González-Romero, A., Klose, M., … & Pérez
839   García-Pando, C. (2022). Insights into the single particle composition, size, mixing state and
840   aspect ratio of freshly emitted mineral dust from field measurements in the Moroccan Sahara
841   using electron microscopy. Atmospheric Chemistry and Physics Discussions, 2022, 1-40.

842 Paulot, F., Ginoux, P., Cooke, W. F., Donner, L. J., Fan, S., Lin, M. Y., … & Horowitz, L. W. (2016).
843   Sensitivity of nitrate aerosols to ammonia emissions and to nitrate chemistry: implications for
844   present and future nitrate optical depth. Atmospheric Chemistry and Physics, 16(3), 1459-
845   1477.

846 Pérez, C., Nickovic, S., Pejanovic, G., Baldasano, J. M., & Özsoy, E.: Interactive dust-radiation modeling:
847   A step to improve weather forecasts. Journal of Geophysical Research: Atmospheres,
848   111(D16), 2006.

849 Pérez García-Pando, C., Stanton, M.C., Diggle, P.J., Trzaska, S., Miller, R.L., Perlwitz, J.P., Baldasano,
850   J.M., Cuevas, E., Ceccato, P., Yaka, P., Thomson, M.C.: Soil dust aerosols and wind as predictors
851   of seasonal meningitis incidence in Niger. Environ. Health Perspect. 122, 7679-686, 2014.

852 Perlwitz, J.P., Pérez García-Pando, C., and Miller, R.L.: Predicting the mineral composition of dust
853   aerosols – Part 1: Representing key processes. Atmos. Chem. Phys., 15, 11593–11627,
854   https://doi.org/10.5194/acp-15-11593-2015, 2015.

855 Potter, C. and Coppernoll-Houston, D.: Controls on land surface temperature in deserts of southern
856   california derived from MODIS satellite time series analysis, 2000 to 2018. Climate, 7, 32,
857   https://doi.org/10.3390/cli7020032, 2019.

Querol, X.: The Occurrence and Distribution of Trace Elements in the Teruel Mining District Coals and their Behaviour during Coal Combustion. European Coal and Steel Community Project 7220/ED/014, 1993.

Querol, X., Whateley, M.K.G., Fernandez-Turiel, J.L., Tuncali, E.: Geological controls on the mineralogy and geochemistry of the Beypazari lignite, Central Anatolia, Turkey. Int. J. Coal. Geol., 33:255–271, 1997.

Raupach, M.R., Gillette, D.A., Leys, J.F.: The effect of roughness elements on wind erosion threshold. J. Geophys. Res., 98, 3023-3029, 1993.

Reheis, M.C., Goodmacher, J.C., Harden, J.W., McFadden, L.D., Rockwell, T.K., Shroba, R.R., Sowers, J.M. and Taylor, E.M. Quaternary soils and dust deposition in southern Nevada and California. Geological Society of America Bulletin, 107(9), pp.1003-1022, 1995.

Reheis, M.C. and Kihl, R. Dust deposition in southern Nevada and California, 1984–1989: Relations to climate, source area, and source lithology. Journal of Geophysical Research: Atmospheres, 100(D5), pp.8893-8918, 1995.

Reheis, M.C. Dust deposition downwind of Owens (dry) Lake, 1991–1994: Preliminary findings. Journal of Geophysical Research: Atmospheres, 102(D22), pp.25999-26008, 1997.

Reheis, M.C., Budahn, J.R. and Lamothe, P.J. Geochemical evidence for diversity of dust sources in the southwestern United States. Geochimica et Cosmochimica Acta, 66(9), pp.1569-1587, 2002.

Reheis, M.C., Budahn, J.R., Lamothe, P.J. and Reynolds, R.L. Compositions of modern dust and surface sediments in the Desert Southwest, United States. Journal of Geophysical Research: Earth Surface, 114(F1), 2009.

Reheis, M.C., Bright, J., Lund, S.P., Miller, D.M., Skipp, G., Fleck, R.J.: A half-million-year record of paleoclimate from the Lake Manix core, Mojave Desert, California. Palaeogeogr., Palaeoclim. Palaeoecol., 365–366, pp. 11-37, 2012.

Reynolds, R.L., Reheis, M., Yount, J. and Lamothe, P. Composition of aeolian dust in natural traps on isolated surfaces of the central Mojave Desert—Insights to mixing, sources, and nutrient inputs. Journal of Arid Environments, 66(1), pp.42-61, 2006.

Reynolds, R.L., Yount, J.C., Reheis, M., Goldstein, H., Chavez Jr, P., Fulton, R., Whitney, J., Fuller, C. and Forester, R.M. Dust emission from wet and dry playas in the Mojave Desert, USA. Earth Surface Processes and Landforms: The Journal of the British Geomorphological Research Group, 32(12), pp.1811-1827, 2007.

Reynolds, R.L., Bogle, R., Vogel, J., Goldstein, H., Yount, J.: Dust emission at Franklin Lake Playa, Mojave Desert (USA): Response to meteorological and hydrologic changes 2005–2008, in: Oren, A., Naftz, D. L., Wurtsbaugh, W. A. (Eds.), Saline lakes around the world: unique systems with unique values, Natural Resources and Environmental Issues 15, 105–116, https://digitalcommons.usu.edu/nrei/vol15/iss1/18 (last access: 7 November 2023), 2009.

Rietveld, H.M.: A profile refinement method for nuclear and magnetic structures. Journal of Applied Crystallography 2, 65–71, 1969.

Scanza, R. A., Mahowald, N., Ghan, S., Zender, C. S., Kok, J. F., Liu, X., ... & Albani, S. (2015). Modeling dust as component minerals in the Community Atmosphere Model: development of framework and impact on radiative forcing. Atmospheric Chemistry and Physics, 15(1), 537-561.

Scarlett, N. & Madsen, I.: Quantification of phases with partial or no known crystal structures. Powder Diffraction, 21(4), 278-284, 2006.

902 Shao, Y., Raupach, M.R., & Findlater, P.A.: Effect of saltation bombardment on the entrainment of dust
903   by wind. Journal of Geophysical Research: Atmospheres, 98(D7), 12719-12726, 1993.

904 Shao, Y. (2001). A model for mineral dust emission. Journal of Geophysical Research: Atmospheres,
905   106(D17), 20239-20254.

906 Shao, Y., Wyrwoll, K. H., Chappell, A., Huang, J., Lin, Z., McTainsh, G. H., ... & Yoon, S. (2011). Dust
907   cycle: An emerging core theme in Earth system science. Aeolian Research, 2(4), 181-204.

908 Shi, Z.B., Krom, M.D., Bonneville, S.: Formation of Iron Nanoparticles and Increase in Iron Reactivity in
909   Mineral Dust during Simulated Cloud Processing. Environ. Sci. Technol. 43, 6592-6596, 2009.

910 Sperazza, M., Moore, J.N., Hendrix, M.: High-Resolution particle size analysis of naturally occurring
911   very fine-grained sediment through laser diffractometry. J. Sediment. Res., 74 (5), 736-743,
912   2004.

913 Stout, J. E., & Lee, J. A. (2003). Indirect evidence of wind erosion trends on the Southern High Plains
914   of North America. Journal of Arid Environments, 55(1), 43-61.

915 Sullivan, R.C., Guazzotti, S.A., Sodeman, D.A., Tang, Y., Carmichael, G.R., & Prather, K.A.: Mineral dust
916   is a sink for chlorine in the marine boundary layer. Atmospheric Environment, 41(34), 7166–
917   7179, 2007.

918 Thorez, J.: Practical Identification of Clay Minerals: A Handbook for Teachers and Students in Clay
919   Mineralogy. Institute of mineralogy, Liège State University, Belgium, Lelotte Eds, B 4820
920   DISON (Belgique),90pg, 1976.

921 Tong, D.Q., Dan, M., Wang, T., Lee, P.: Long-term dust climatology in the western United States
922   reconstructed from routine aerosol ground monitoring, Atmos. Chem. Phys., 12, 5189–5205,
923   https://doi.org/10.5194/acp-12-5189-2012, 2012.

924 TOPAS: TOPAS and TOPAS-Academic: an optimization program integrating computer algebra and
925   crystallographic objects written in C++. J. Appl. Cryst. (2018). 51, 210-218, 2018.

926 Urban, F.E., Reynolds, R.L., Fulton, R.: The dynamic interaction of climate, vegetation, and dust
927   emission, Mojave Desert, USA. A. Fernandez-Bernal, M.A. De La Rosa (Eds.), Arid
928   Environments and Wind Erosion, NOVA Science Publishers, Inc., pp. 243-267, 2009.

929 Urban, F.E., Goldstein, H.L., Fulton, R., Reynolds, R.L.: Unseen dust emission and global dust
930   abundance: documenting dust emission from the Mojave Desert (USA) by daily remote
931   camera imagery and wind-erosion measurements. J. Geophys. Res. Atmos., 123 (16), pp.
932   8735-8753, 2018.

933 USGS, U. S. Geological Survey Open-File Report 01-041. A Laboratory Manual for X-Ray Powder
934   Diffraction https://pubs.usgs.gov/of/2001/of01-041/htmldocs/methods/oamount.htm. Last
935   access: 17th January of 2024.

936 Vandenberghe, R. E., Barrero, C. A., Da Costa, G. M., Van San, E., and De Grave, E.: Mössbauer
937   characterization of iron oxides and (oxy) hydroxides: the present state of the art. Hyperfine
938   Interactions, 126, 247-259, 2000.

939 Weaver, C., Ginoux, P., Hsu, N., Chou, M.-D., Joiner, J.: Radiative forcing of Saharan dust: GOCART
940   model simulations compared with ERBE data. J. Atmos. Sci., 59, 736-747, 2002.

941 Whitney, J.W., Breit, G.N., Buckingham, S.E., Reynolds, R.L., Bogle, R.C., Luo, L., Goldstein, H.L., Vogel,
942   J.M.: Aeolian responses to climate variability during the past century on Mesquite Lake Playa,
943   Mojave Desert. Geomorphology, 230, 13-25, 2015.

944 Young, R.A.: The Rietveld method. International Union of Crystallography. Oxford University Press, UK,
945   1993.

946 Zubko, N., Munoz, O., Zubko, E., Gritsevich, M., Escobar-Cerezo, J., Berg, M. J. and Peltoniemi, J.: Light
947   scattering from volcanic-sand particles in deposited and aerosol form. Atmospheric
948   Environment, 215, 116813. https://doi.org/10.1016/j.atmosenv.2019.06.051, 2019.

949 **Figure captions:**

950 **Figure 1:** Study area map including the playa lakes studied together with a geologic map, simplified
951 from Jennings et al. (1962) and Miller et al. (2014). The star represents the Zzyzx complex and green
952 dots the samples used in this study. Basemap: Imagery data from © Google Earth Pro v: 7.3.6.9345.

953 **Figure 2:** Map of Frequency of Occurrence (FoO) of dust optical depth > 0.1 over the study region
954 derived from MODIS C6.1 Aqua (1:30PM equatorial passing time) Level 2 Deep Blue aerosol products
955 at 0.1 degree resolution. A dust occurrence is counted when DOD > 0.1, Angstrom Exponent < 0.3 and
956 DOD at 412 nm > DOD at 470 nm. Blue iso-contours represent 5 and 10 % of daily occurrences per
957 year averaged over 20 years (2003-2022). Green dots represent the samples collected and used in this
958 study. Basemap: Imagery data from © Google Earth Pro v: 7.3.6.9345.

959 **Figure 3:** EMIT scenes emit20231015T215209_color-visRGB and emit20230728T214142_color-visRGB
960 at 60 m per pixel showing the diversity of Fe^{2+}, Fe^{3+} and Fe^{2+} and Fe^{3+} bearing minerals and the
961 carbonates, salt and phyllosilicates minerals.

962 **Figure 4:** Examples of samples collected in the Mojave Desert including crusts (a), aeolian ripples (b),
963 massive compact crust (c) and a salty spongy crust (d).

964 **Figure 5:** Fully dispersed particle size distribution (FDPSD) and minimally dispersed particle size
965 distribution (MDPSD) for crusts and aeolian ripples from the Mojave Desert (median PSD from all the
966 samples), Soda, Mesquite, Cronese, Ivanpah and Coyote Lakes. In shaded blue and brown the standard
967 deviation of each PSD (nº of samples used in Table 1), except for Ivanpah and Coyote Lakes (only 1
968 sample each).

969 **Figure 6:** % of mass fractions from the dry sieved size fractions (250-50, 80-250, 63-80, 40-63, 20-40
970 and <20 μm). The range of the enrichment factors of each mineral group for each dry size fraction of
971 the 16 crust samples (blue) and for the 4 aeolian ripples samples (red).

972 **Figure 7:** Box-plot showing averaged mineral contents for all samples, crusts and aeolian ripples (wt
973 %).

974 **Figure 8:** Geological cross section and mineralogy of the crusts of the Soda Lake. Top panel represent
975 major mineralogy composition. Mid panel represents the position of the samples, the Zzyzx complex,
976 and the path of the cross section. Bottom schematic cross section simplifying the position in the basin.
977 Basemap: Imagery data from © Google Earth Pro v: 7.3.6.9345.

978 **Figure 9:** Cross-correlation plots of the clay contents and amphibole with the FeT (a) and clay minerals
979 and FeA (b), all in wt % in crusts.

980 **Figure 10:** Modes of occurrence of Fe comparison between the crusts (C) playa lakes analysed in this
981 study, the average of the crusts and ripples (R) at Mojave Desert, Morocco and Iceland Top surface
982 (TS). FeA is referred to the exchangeable Fe and nano Fe oxides, FeD is the Fe content in hematite and
983 goethite, FeM is the Fe content in maghemite/magnetite and FeS is the Fe content in Fe bearing
984 minerals.

985 **Figure 11:** Conceptual model of wet and dry playa lakes differences due to groundwater differences
986 and how this can affect the mineralogy of the surface in the playa lakes. Also illustrated is the expected
987 dust emission rate, major mineralogy and modes of occurrence of Fe differences expected in the
988 emitted dust.

989

990   Figure 1.
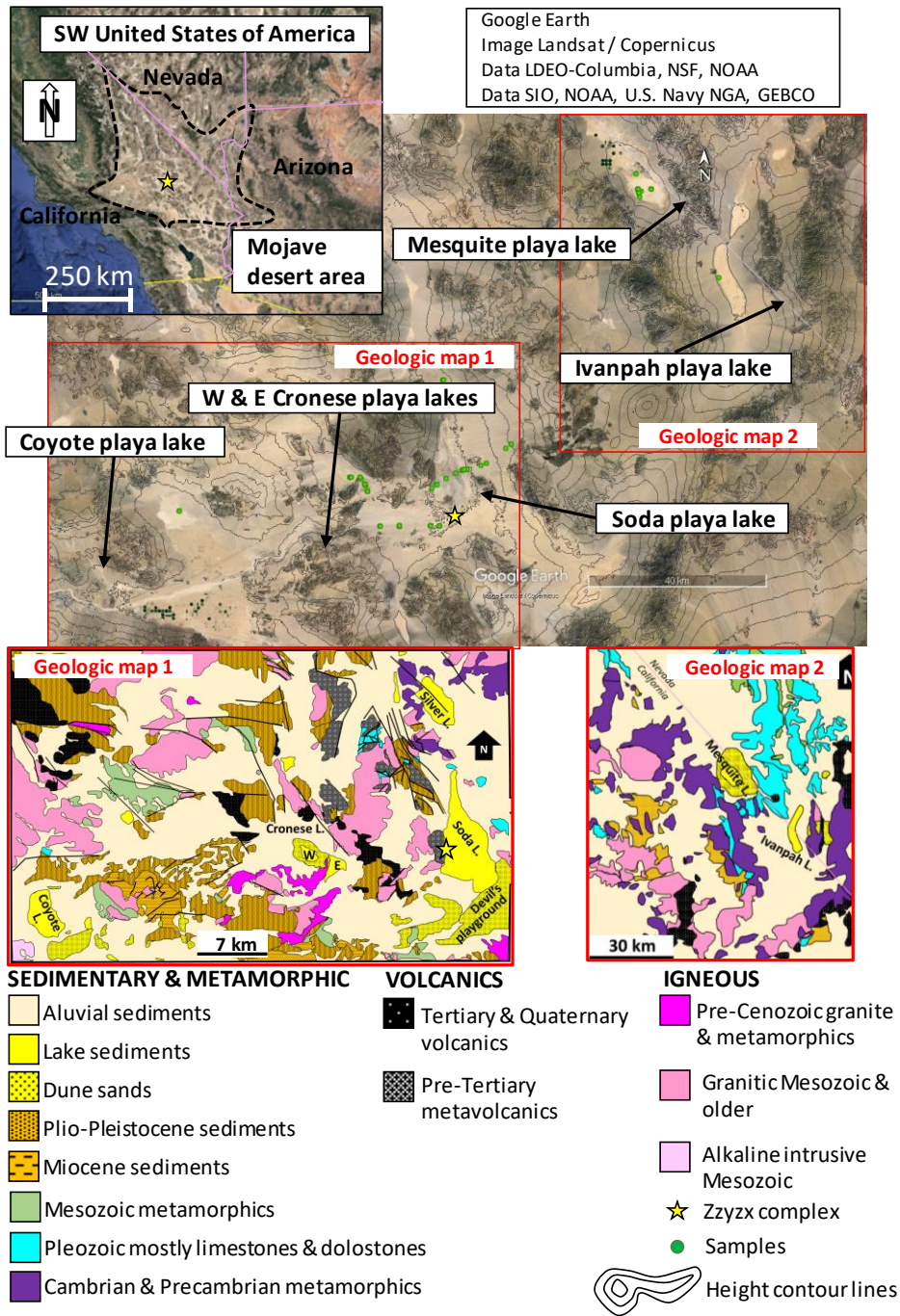
991

992

993

994

995

996

997

998   Figure 2.

999
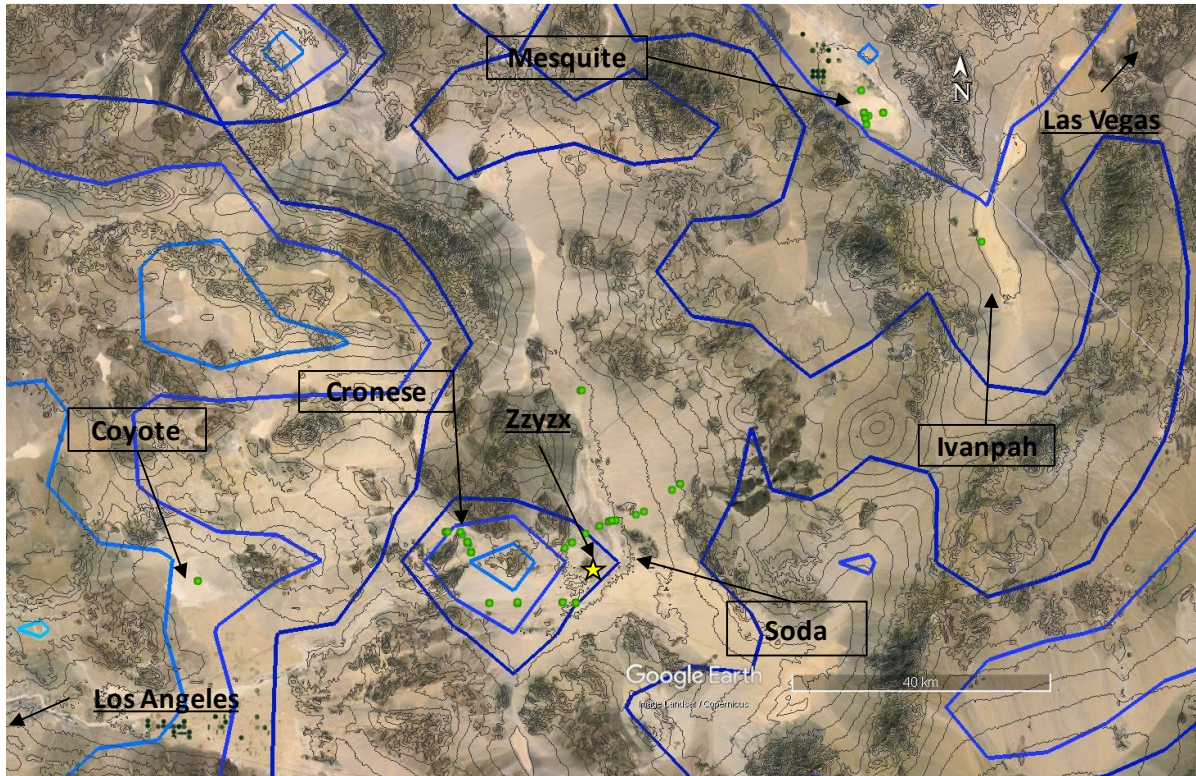
1000
1001
1002
1003
1004
1005
1006
1007
1008
1009
1010
1011
1012
1013
1014
1015
1016
1017
1018
1019
1020
1021
1022

1023   Figure 3.
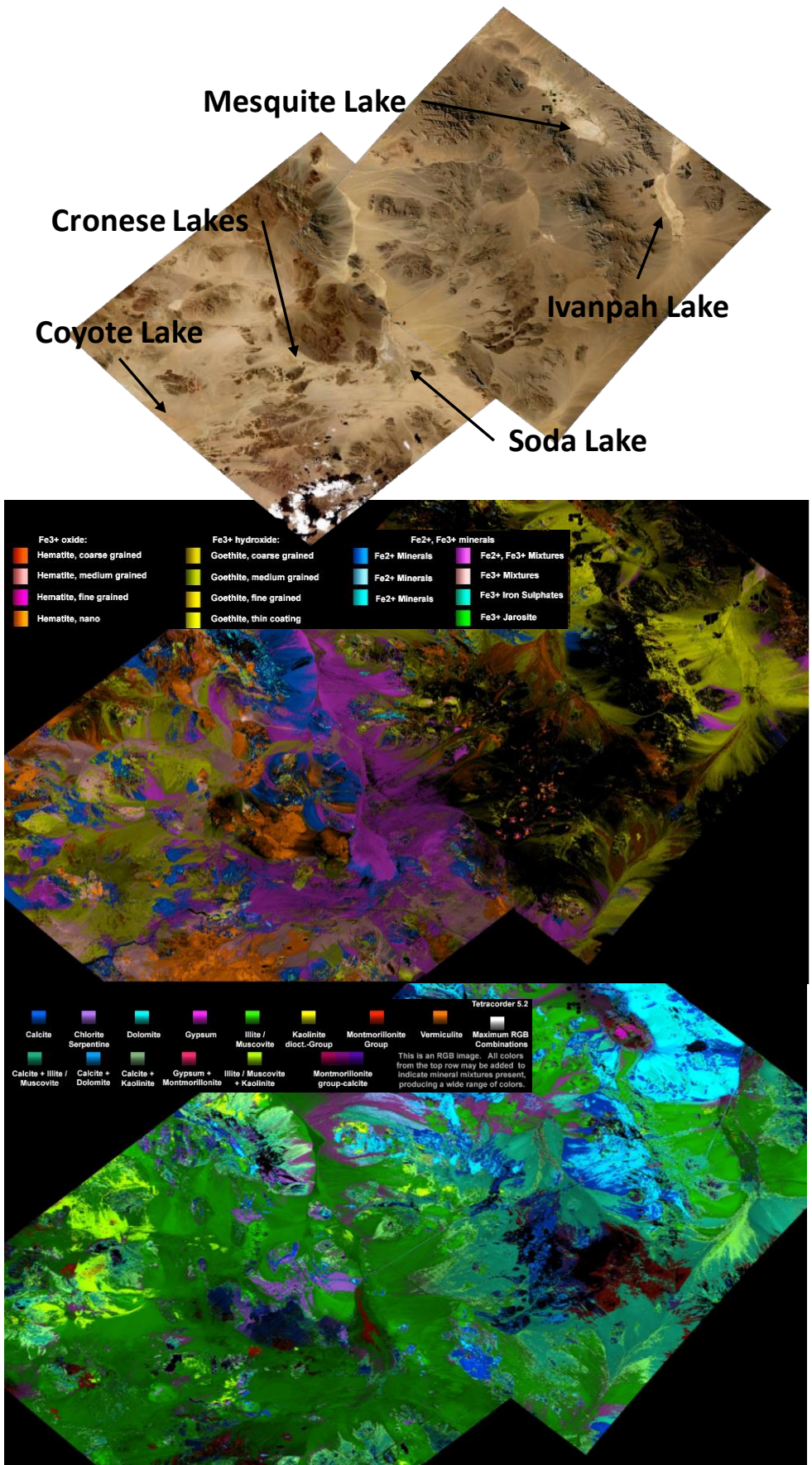
1025   Figure 4.
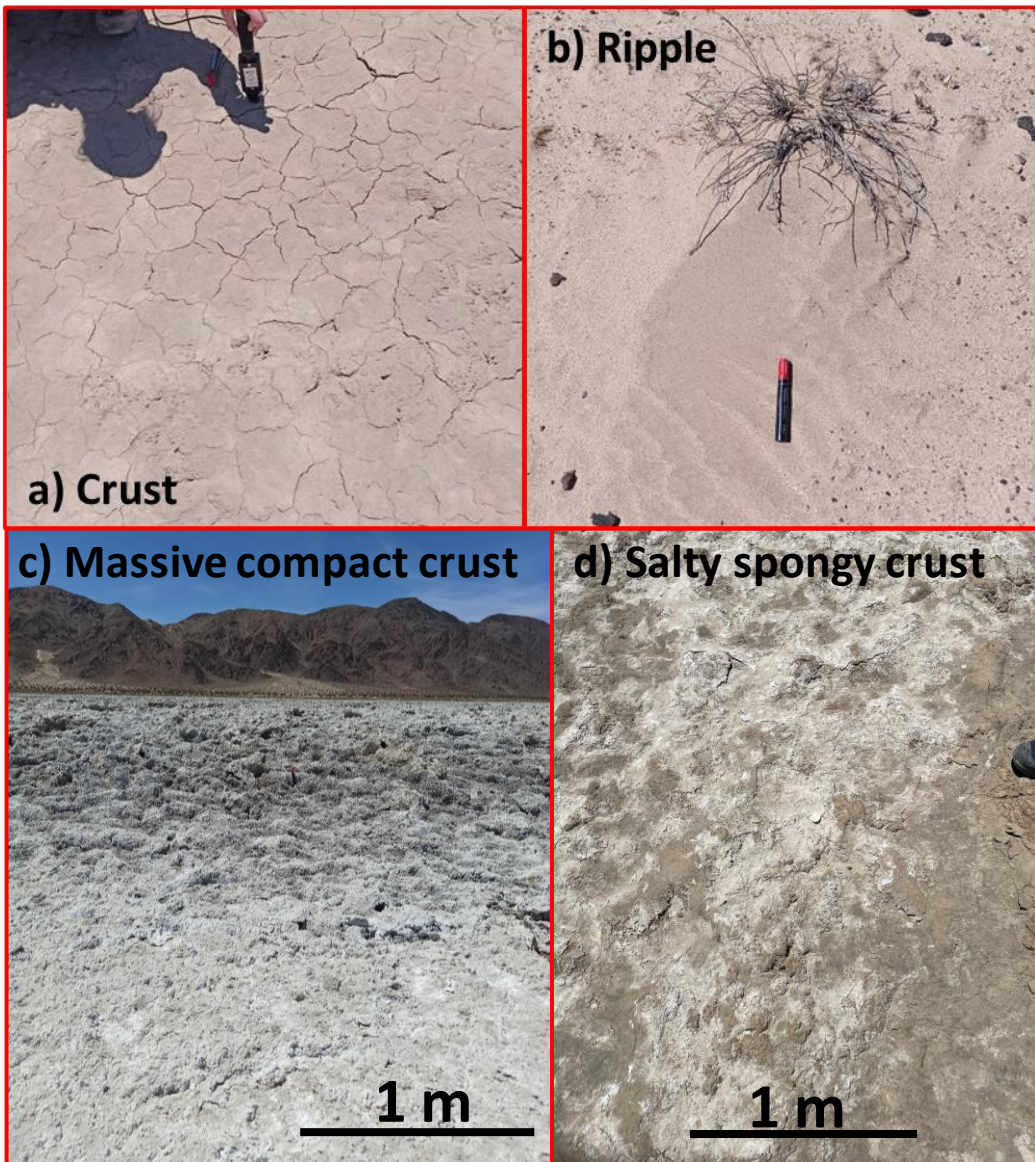
1026

1027

1028
1029
1030
1031
1032
1033
1034
1035
1036
1037
1038
1039
1040

1041   Figure 5.
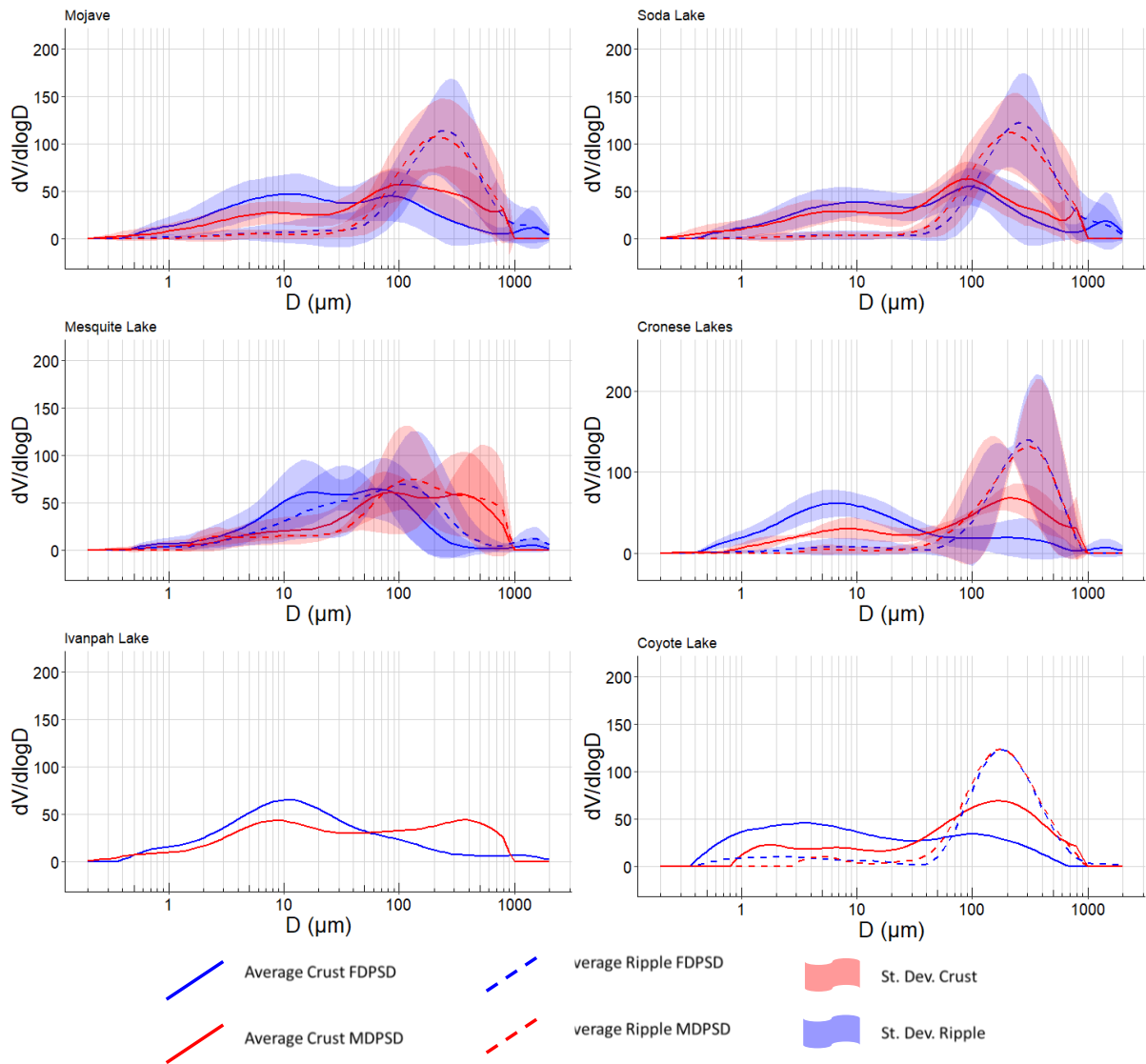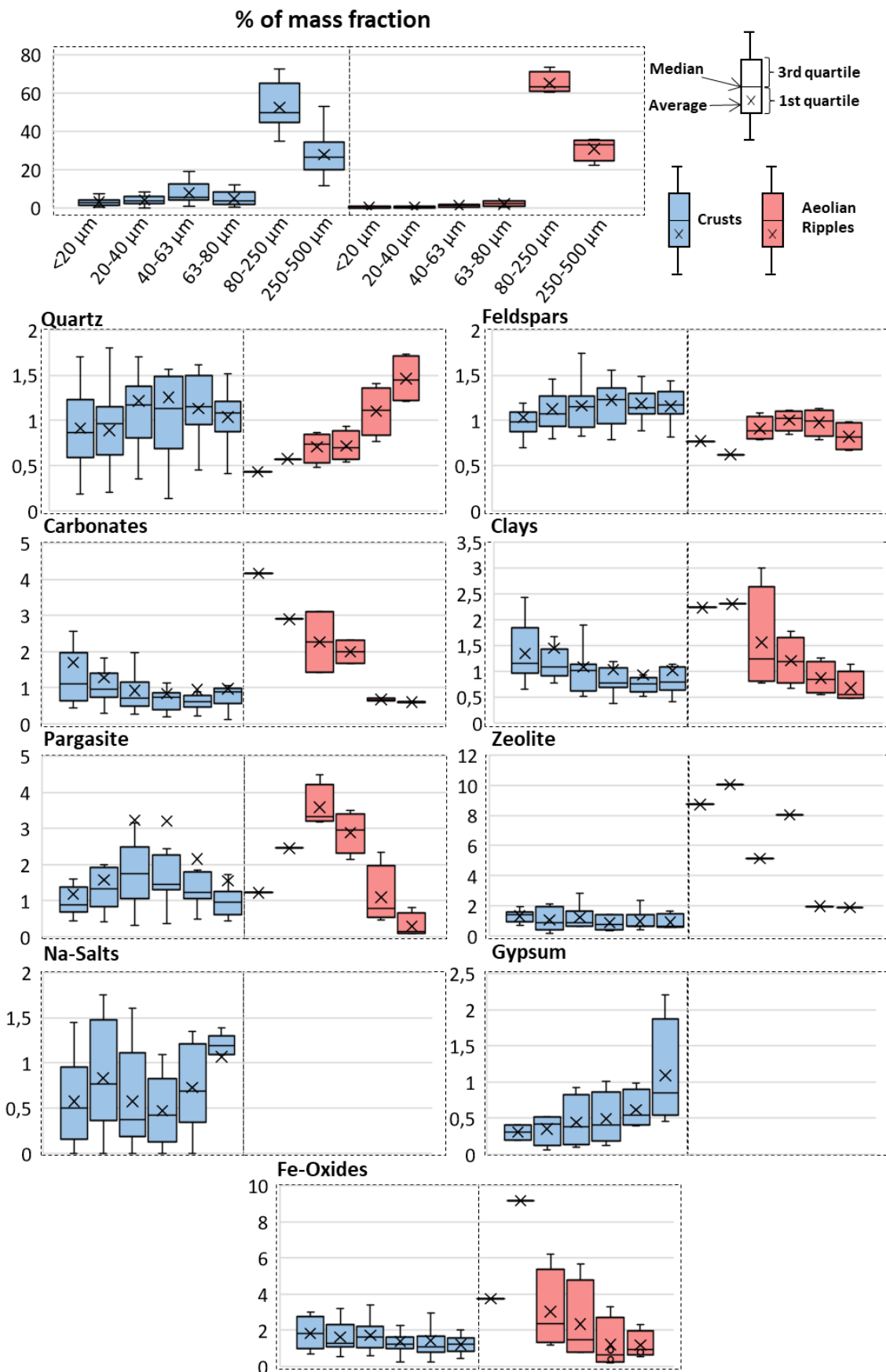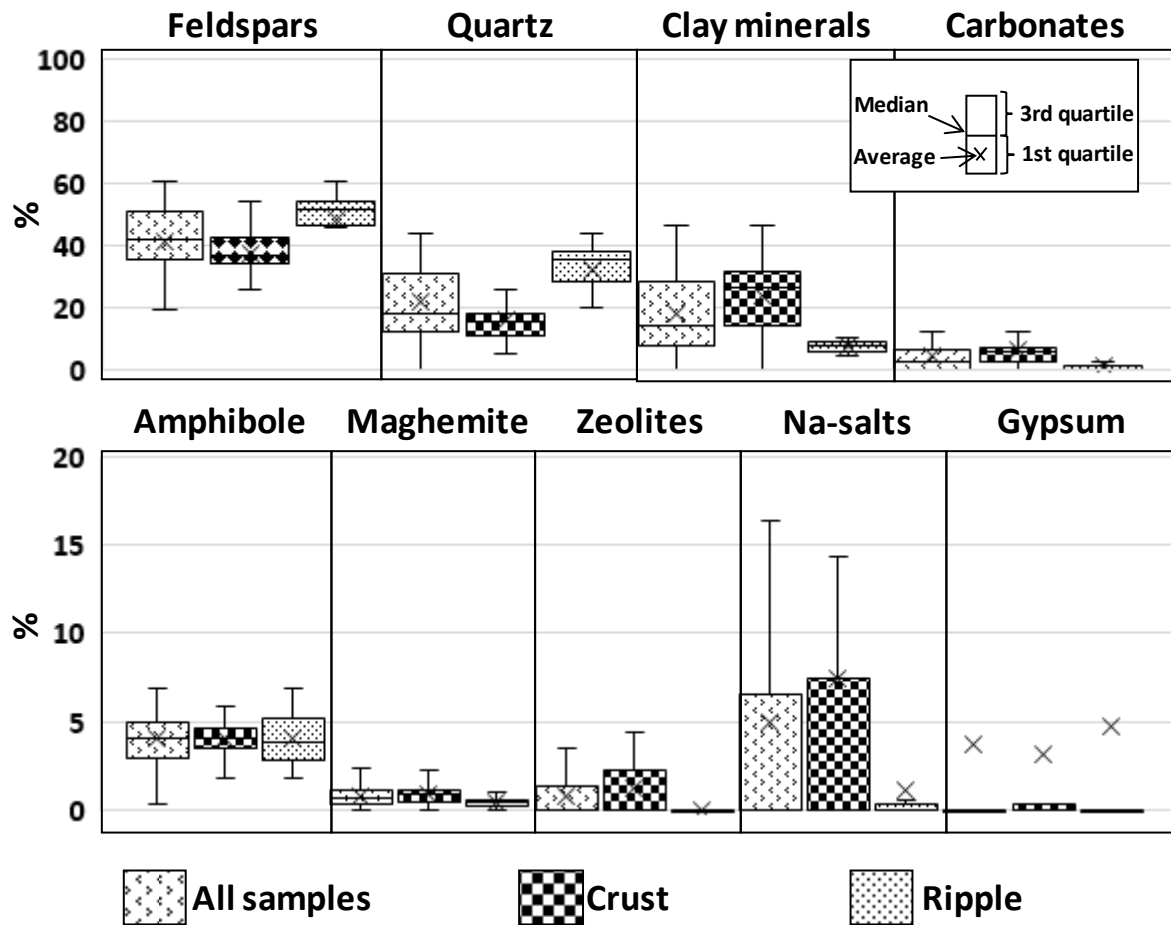
Figure 7.

1077   Figure 8.
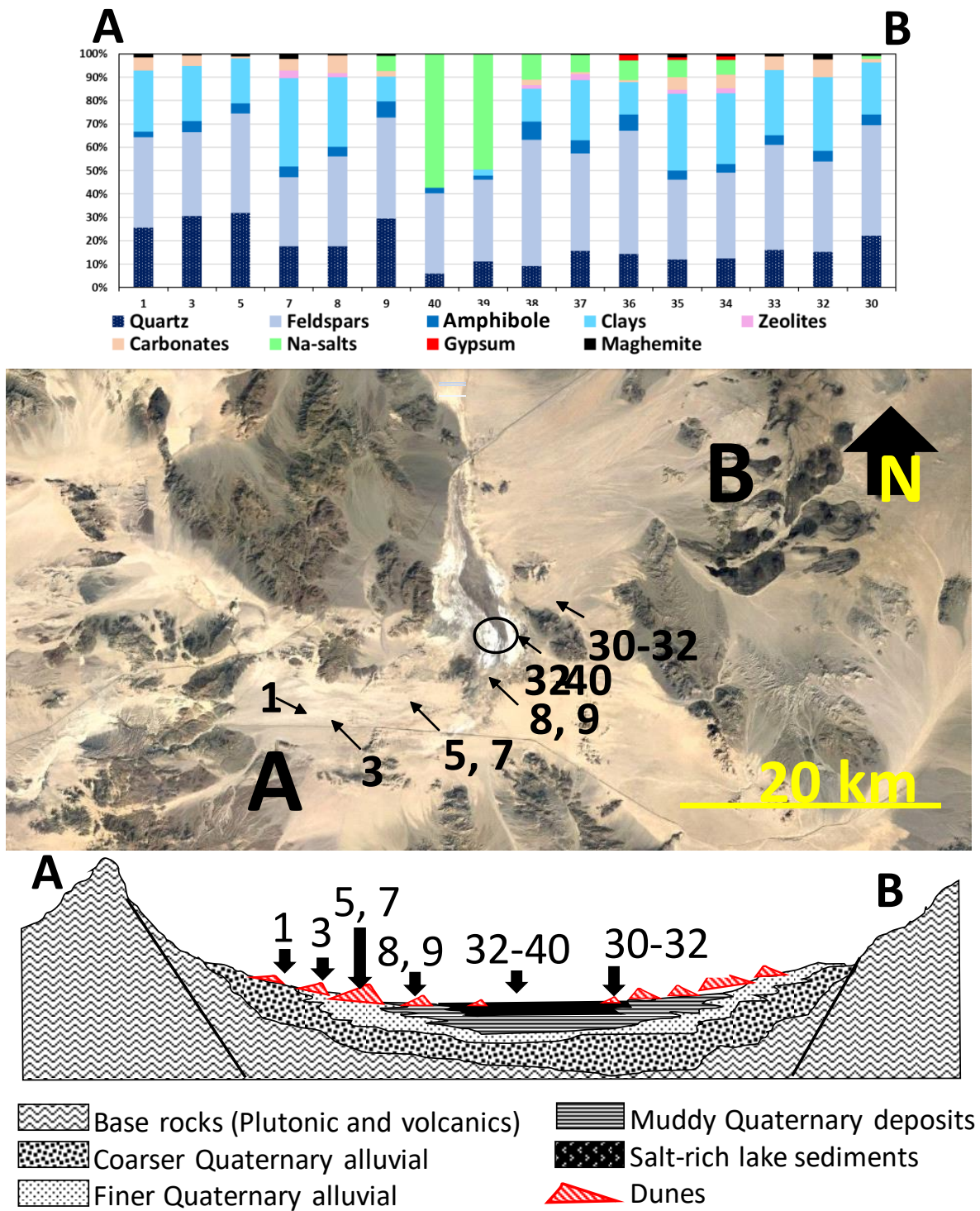
1078

1079

1080

1081

1082

1083   Figure 9.
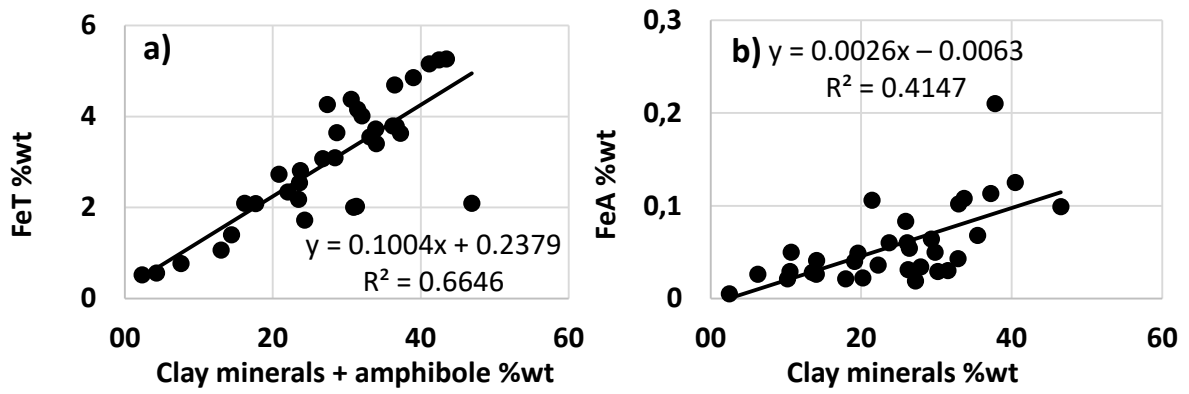
1084

1085

1086

1087

1088

1089

1090

1091

1092

1093

1094

1095

1096

1097

1098

1099

1100

1101

1102

1103

1104

1105

1106   Figure 10.
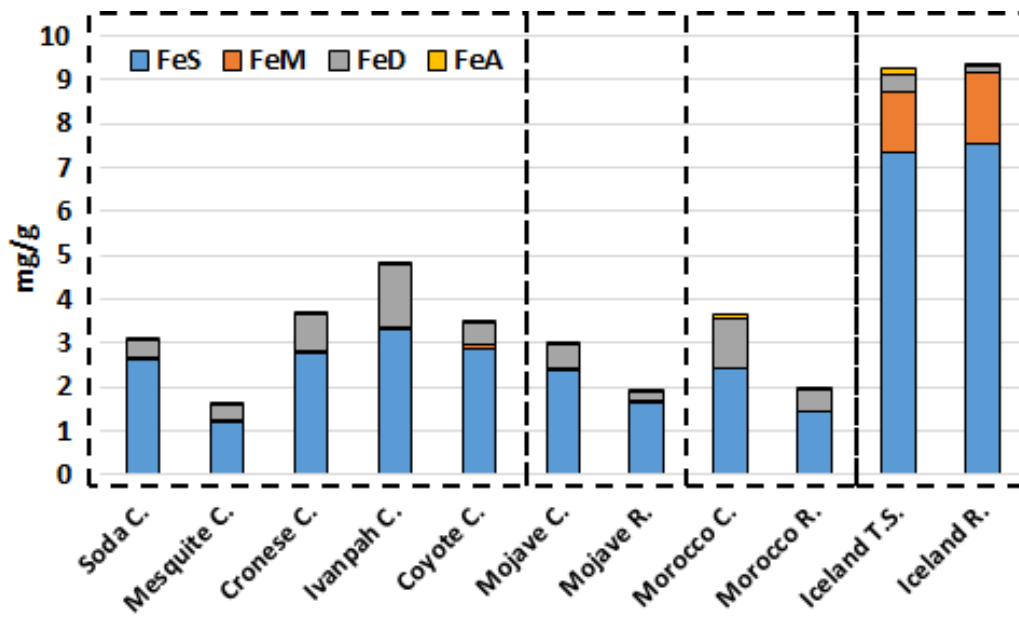
1107

1108

1109

1110

1111

1112

1113

1114

1115

1116

1117

1118

1119

1120

1121

1122

1123

1124
1125
1126

 Figure 11.
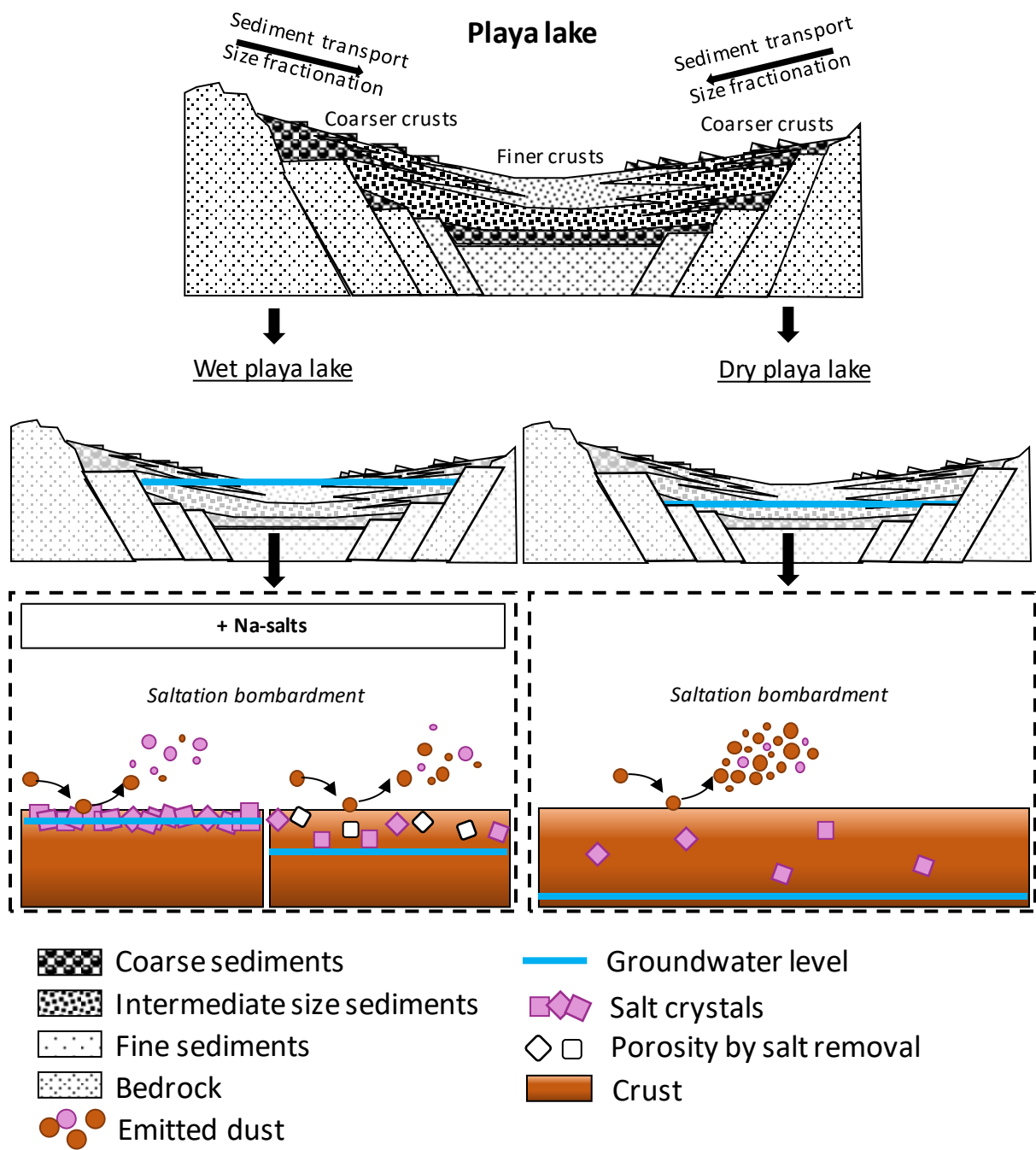
1138 Table 1. Full range (<2000 μm), <63μm and >63 to 2000 μm mean diameter, standard deviation, min.,
1139 and max for minimally dispersed particle size distribution (MDPSD) and fully dispersed particle size
1140 distribution (FDPSD).

Surface	Location	N	MDPSD		
			Full range	≤ 63 μm	>63 to 2000 μm
			Mean of medians ± Std. Dev. [Min,Max]		
Crusts	Mojave	35	92 ± 74 [10,349]	22 ± 6.4 [11,34]	254 ± 71 [155,489]
Ripples		20	226 ± 88 [88, 418]	37 ± 6.0 [20,46]	276 ± 80 [130,424]
Crusts	Soda	17	63 ± 47 [10,156]	21 ± 6.5 [11,31]	234 ± 82 [155,489]
	Cronese	9	109 ± 60 [35,195]	18 ± 2.2 [15,22]	280 ± 40 [238,357]
	Mesquite	7	141 ± 117 [31,349]	28 ± 5.6 [21,34]	257 ± 79 [157,387]
	Ivanpah	1	35 ± NA [35,35]	16 ± NA [16,16]	314 ± NA [314,314]
	Coyote	1	101 ± NA [101,101]	20 ± NA [20,20]	254 ± NA [254,254]
Ripples	Soda	15	231 ± 87 [88,418]	39 ± 3.5 [29,43]	275 ± 77 [130,424]
	Cronese	2	264 ± 147 [160,368]	40 ± 8.8 [34,46]	292 ± 120 [208,377]
	Mesquite	2	167 ± 112 [110,225]	26 ± 8.9 [20,32]	286 ± 146 [183,389]
	Ivanpah	0	NA	NA	NA
	Coyote	1	179 ± NA [179,179]	32 ± NA [32,32]	236 ± NA [236,236]
Surface	Location	N	FDPSD		
			Full range	≤ 63 μm	>63 to 2000 μm
			Mean of medians ± Std. Dev. [Min,Max]		
Crusts	Mojave	35	37 ± 48 [4.9,240]	18 ± 6.6 [8.4,35]	306 ± 237 [106,1093]
Ripples		20	213 ± 92 [28,362]	29 ± 8.3 [15,48]	335 ± 99 [213,561]
Crusts	Soda	17	52 ± 61 [8.4,240]	19 ± 5.3 [12,27]	321 ± 212 [113,815]
	Cronese	9	17 ± 23 [4.9,77]	12 ± 3.1 [8.4,19]	381 ± 345 [144,1093]
	Mesquite	7	34 ± 28 [11,91]	24 ± 7.7 [16,35]	185 ± 104 [106,336]
	Ivanpah	1	12 ± NA [21,21]	15 ± NA [15,15]	347 ± NA [347,347]
	Coyote	1	8.4 ± NA [8.4,8.4]	12 ± NA [12,12]	187 ± NA [187,187]
Ripples	Soda	15	234 ± 82 [92,362]	31 ± 7.9 [21,48]	346 ± 97 [238,561]
	Cronese	2	236 ± 126 [147,325]	18 ± NA [18,18]	295 ± 108 [219,371]
	Mesquite	2	67 ± 56 [28,107]	27 ± 3.5 [24,29]	336 ± 173 [213,458]
	Ivanpah	0	NA	NA	NA
	Coyote	1	156 ± NA [156,156]	15 ± NA [15,15]	245 ± NA [245,245]

1141

1142

1143

1144

1145

1146

1147

1148

1149

1150

1151 Table 2. Average and standard deviations of the mineral contents (wt %) from crust and aeolian ripple
1152 samples from the Mojave Desert and the different study basins. NaN, not a number. Maghemite is
1153 considered as Maghemite and Magnetite

	Clays	Carbonate	Salts	Zeolites	Maghemite	Quartz	Feldspars	Gypsum	Amphibole
CRUSTS	24±11	6.6±6.6	7.3±13	1.2±1.9	0.92±0.59	16±7.2	37±9.7	3.1±14	4.1±1.5
Soda	22±11	3.6±2.6	8.9±17	0.77±1.1	0.97±0.66	18±7.7	40±6.7	0.29±0.68	4.5±1.6
Cronese	31±11	5.4±1.8	2.2±3.4	2.4±1.7	1.0±0.28	14±7.3	40±5.5	<0.1	3.4±1.5
Coyote	28	7,2	1,2	8,5	0,48	11	37	<0.1	5.6
Ivanpah	36	6.9	<0.1	<0.1	1,2	15	36	<0.1	3.5
Mesquite	17±8.2	15±11	12±14	<0.1	0.71±0.75	14±5.8	24±12	15±29	2.8±1.4
RIPPLES	7.8±2.3	1.1±2.2	1.1±3,7	0.12±0.52	0.49±0.28	32±9.5	48±13	4.7±20	4.1±1.6
Soda	7.4±1.8	0.47±0.73	0.19±0.46	<0.1	0.49±0.25	35±4.5	52±4.7	<0.1	4.3±1.5
Cronese	8.4±0.60	1.2±1.7	<0.1	<0.1	0.83±0.33	32±9.0	53±0.03	<0.1	4.7±3.2
Coyote	7.9	2.3	<0.1	2,3	0.60	28	52	<0.1	3.5
Ivanpah	NaN	NaN	NaN	NaN	NaN	NaN	NaN	NaN	NaN
Mesquite	10±6.1	4.8±6.8	9.4±9.9	<0.1	0.19±0.27	10±14	15±21	47±60	3.7±1.5

1154

1155
1156
1157
1158
1159
1160
1161
1162
1163
1164
1165
1166
1167
1168
1169
1170
1171
1172
1173
1174
1175
1176
1177
1178
1179
1180

1182 Table 3. Fe content in wt % for total Fe (FeT) content, and in % for ascorbate Fe (FeA), dithionite (FeD),

1183 oxalate Fe (FeM) and structural Fe (FeS). NaN not a number.

	FeT	FeA %	FeD %	FeM %	FeS %
CRUSTS	3.0±1.3	1.8±0.92	17±7.2	2.1±1.2	79±8.5
Soda	3.1±1.2	1.5±0.81	14±2.5	1.5±0.49	83±2.8
Cronese	3.7±1.2	2.4±0.99	21±11	2.3±1.1	74±13
Coyote	3.5	1.8	14	2.4	82
Ivanpah	4.9	1.4	29	0.82	68
Mesquite	1.6±0.53	1.8±0.93	20±2.7	3.7±1.2	74±3.5
RIPPLES	1.9±1.1	1.4±1.2	12±5.6	2.4±1.8	84±7.5
Soda	2.0±1.2	0.98±0.39	10±3.4	2.1±1.8	87±4.4
Cronese	2.3±1.5	1.4±0.35	14±9.3	2.8±2.9	82±12
Coyote	1.3	3.4	26	3.0	68
Ivanpah	NaN	NaN	NaN	NaN	NaN
Mesquite	1.0±1.1	3.6±3.0	20±1.2	4.4±1.2	73±4.1

1211 Table 4. Summarise MDPSD (µm), FDPSD (µm) median particle diameter, Quartz (Qtz, wt %), feldspars
1212 (Feld., wt %), clay mineral (Clay, wt %), carbonates (Carb., wt %), Na-salts (Na-S, wt %), Gypsum (Gp,
1213 wt %), total Fe content (FeT, wt %), exchangeable Fe (FeA, wt %), dithionite Fe (Hematite and Goethite,
1214 wt %), oxalate Fe (FeM, wt %) and structural Fe (FeS, wt %) for Mojave and Morocco crusts and Iceland
1215 top sediments. NaN not a number.
1216

	MDPSD d(0.5)	FDPSD d(0.5)	Qtz	Feld.	Clay	Carb.	Na-S	Gp	FeT	FeA	FeD	FeM	FeS
Mojave	92	37	16	37	24	6.6	7.3	3.1	3.0	0.06	0.53	0.06	2.4
Morocco	113	37	48	9.4	17	22	7.0	0.64	3.6	0.07	1.1	NaN	2.4
Iceland	55	56	0.21	20	NaN	NaN	NaN	NaN	9.3	0.15	0.43	1.4	7.3

1217
1218
1219